Gamma-rays and Neutrinos from Cosmic Accelerators

Contents

1 Topics

- High energy gamma-ray emission from galactic and extragalctic sources
- Galactic sources of high energy neutrinos

1.1 ICRANet participants

- Aharonian Felix
- Sahakyan Narek

1.2 Students

- Zargaryan David
- Baghmanyan Vardan

1.3 Ongoing collaborations

- Francesco Vissani (INFN, Gran Sasso Theory Group, Italy)
- Marco Tavani (INAF-IASF Roma and Universit di Roma "Tor Vergata", Italy)
- Frank Rieger (Max-Planck-Institut für Kernphysik, Germany)
- Rui-zhi Yang (Key Laboratory of Dark Matter and Space Astronomy, China)
- Giovanni Piano (INAF-IASF Roma, INFN Roma and Univ. Tor Vergata, Italy)

2 Brief description

The works done and currently being developed within our group lie in the field of particle astrophysics including high energy gamma and neutrino astrophysics. The detection of these particles gives the opportunity to understand the physical processes that occur in astrophysical sources: they are not affected by interaction with extragalactic and galactic electromagnetic fields before they reach the Earth, and therefore point directly to the source of emission.
Below we present several abstracts from the papers published in 2014.

- Hadronic HE γ-ray and ν emission from Cygnus X-3

Cygnus X-3 (Cyg X-3) is a remarkable Galactic microquasar (X-ray binary) emitting from radio to γ-ray energies. In this paper, we consider hadronic model of emission of γ-rays above 100 MeV and their implications. We focus here on the joint γ-ray and neutrino production resulting from proton-proton interactions within the binary system. We find that the required proton injection kinetic power, necessary to explain the γ-ray flux observed by AGILE and *Fermi*-LAT, is $L_p \sim 10^{38}\,\mathrm{erg\,s^{-1}}$, a value in agreement with the average bolometric luminosity of the hypersoft state (when Cygnus X-3 was repeatedly observed to produce transient γ-ray activity). If we assume an increase of the wind density at the superior conjunction, the asymmetric production of γ-rays along the orbit can reproduce the observed modulation. According to observational constraints and our modelling, a maximal flux of high-energy neutrinos would be produced for an initial proton distribution with a power-law index $\alpha = 2.4$. The predicted neutrino flux is almost two orders of magnitude less than the 2-month IceCube sensitivity at $\sim$1 TeV. If the protons are accelerated up to PeV energies, the predicted neutrino flux for a prolonged "soft X-ray state" would be a factor of about 3 lower than the 1-year IceCube sensitivity at $\sim$10 TeV. This study shows that, for a prolonged soft state (as observed in 2006) possibly related with γ-ray activity and a hard distribution of injected protons, Cygnus X-3 might be close to being detectable by cubic-kilometer neutrino telescopes such as IceCube.

- On the gamma-ray emission from 3C 120

We report the analysis of Fermi Large Area Telescope data from five years of observations of the broad line radio galaxy 3C 120. The accumulation

of larger data set results in the detection of high-energy γ-rays up to 10 GeV, with a detection significance of about 8.7σ. A power-law spectrum with a photon index of 2.72 ± 0.1 and integrated flux of $F_\gamma = (2.35 \pm 0.5) \times 10^{-8}$ photon cm$^{-2}s^{-1}$ above 100 MeV well describe the data averaged over five year observations. The variability analysis of the light curve with 180-, and 365- day bins reveals flux increase (nearly twice from its average level) during the last year of observation. During this period the short time interval of source detectability (7- days) indicates the compactness of the emitting region. The γ-ray spectrum can be described as synchrotron self-Compton (SSC) emission from the electron population producing the radio-to-X-ray emission in the jet. The required electron energy density exceeds the one of magnetic field only by a factor of 10 meaning no significant deviation from equipartition.

- Hadronic gamma-rays from RX J1713.7-3946?

RX J1713.7-3946 is a key object to check the supernova remnant paradigm of the origin of Galactic cosmic rays. While the origin of its gamma–ray emission (hadronic versus leptonic) is still debated, the hard spectrum at GeV energies reported by the *Fermi* collaboration is generally interpreted as a strong argument in favor of a leptonic scenario. On the contrary, we show that hadronic interactions can naturally explain the gamma–ray spectrum if gas clumps are present in the supernova remnant shell. The absence of thermal X–rays from the remnant fits well within this scenario.

- The Fermi bubbles revisited

We analyze 60 months of all-sky data from the Fermi-LAT. The Fermi bubble structures discovered previously are clearly revealed by our analysis. With more data, hence better statistics, we can now divide each bubble into constant longitude slices to investigate their gross ?-ray spectral morphology. While the detailed spectral behavior of each slice derived in our analysis is somewhat dependent on the assumed background model, we find, robustly, a relative deficit in the flux at low energies (i.e., hardening) toward the top of the south bubble. In neither bubble does the spectrum soften with longitude. The morphology of the Fermi bubbles is also revealed to be energy-dependent: at high energies they are more extended. We conclude from the gamma-ray spectrum at high latitudes that a low energy break in the parent cosmic ray population is required in both leptonic and hadronic models. We briefly discuss possible leptonic and hadronic interpretations of this phenomenology.

3 Publications-2014

- Gabici, S. and Aharonian, F. "Hadronic gamma-rays from RX J1713.7-3946?", Monthly Notices of the Royal Astronomical Society: Letters, Volume 445, Issue 1, L70, 2014.
- Yang, Rui-zhi, Aharonian, F. and Crocker, R. "The Fermi bubbles revisited", Astronomy & Astrophysics, Volume 567, id.A19, 2014.
- Yang, Rui-zhi, de Ona Wilhelmi, E. and Aharonian, F. "Probing cosmic rays in nearby giant molecular clouds with the Fermi Large Area Telescope", Astronomy & Astrophysics, Volume 566, id. A142, 2014.
- Kelner, S., Lefa, E., Rieger, F. and Aharonian, F. "The Beaming Pattern of External Compton Emission from Relativistic Outflows: The Case of Anisotropic Distribution of Electrons", The Astrophysical Journal, Volume 785, Issue 2, id. 141, 2014.
- Zirakashvili, V., Aharonian, F., Yang, R., Ona-Wilhelmi, E. and Tuffs, R. "Nonthermal Radiation of Young Supernova Remnants: The Case of CAS A", The Astrophysical Journal, Volume 785, Issue 2, id. 130, 2014.
- Khangulyan, D., Aharonian, F. and Kelner, S. "Simple Analytical Approximations for Treatment of Inverse Compton Scattering of Relativistic Electrons in the Blackbody Radiation Field", The Astrophysical Journal, Volume 783, Issue 2, id. 100, 2014.
- Sahakyan, N., Piano, G. and Tavani, M. "Hadronic Gamma-Ray and Neutrino Emission from Cygnus X-3", The Astrophysical Journal, Volume 780, Issue 1, article id. 29, 2014.
- Sahakyan, N., Rieger, F., Aharonian, F., Yang, R., and de Ona-Wilhelmi, E. "On the gamma-ray emission from the core and radio lobes of the radio galaxy Centaurus A", International Journal of Modern Physics: Conference Series, Volume 28, id. 1460182, 2014.
- Sahakyan, N. " Galactic sources of high energy neutrinos", EPJ Web of Conferences, RICAP-14 proceedings, 2014.
- Sahakyan, N., Zargaryan, D. and Baghmanyan, V. "On the gamma-ray emission from 3C 120", submitted to Astronomy and Astrophysics, 2014.

3.1 Publications-2007-2012

- Sahakyan, N., Yang, R. Aharonian, F. and Rieger, F., " Evidence for a Second Component in the High-energy Core Emission from Centaurus A?", The Astrophysical Journal Letters, Volume 770, Issue 1, L6, 2013.
- Yang, R.-Z., Sahakyan, N., de Ona Wilhelmi, E., Aharonian, F. and Rieger, F., "Deep observation of the giant radio lobes of Centaurus A with the Fermi Large Area Telescope", Astronomy & Astrophysics, 542, A19, 2012.
- Sahakyan, N., "High energy gamma-radiation from the core of radio galaxy Centaurus A", Astrophysics, 55, 14, 2012.
- Sahakyan, N., "On the Origin of High Energy Gamma-Rays from Giant Radio Lobes Centarus A", International Journal of Modern Physics Conference Series, 12, 224, 2012.
- Vissani, F., Aharonian, F. and Sahakyan, N.,"On the detectability of high-energy galactic neutrino sources", Astroparticle Physics, 34, 778, 2011.

4 Hadronic HE γ-ray and ν emission from Cygnus X-3

4.1 Introduction

Cyg X-3 was discovered in 1966 [25] as a bright X-ray source. It is a high-mass X-ray binary (HMXB) located at an estimated distance of about 7-10 kpc [15, 37]. The donor star is known to be a Wolf-Rayet (WR) star [56] with a strong helium stellar wind [52], while it's still unclear whether the accreting object is a neutron star or a stellar black hole [57], even though a black hole scenario is favored [52, 53]. The orbital period – detected in infrared [14], X-ray [42], and γ-ray [23] bands – is very short (4.8 hours), indicating that the compact object is completely enshrouded in the wind of the companion star (orbital distance, $d \approx 3 \times 10^{11}$ cm). Cyg X-3 is known to produce giant radio outburst ("major radio flares") up to a few tens of Jy. During these huge flares, milliarcsec-scale observations at cm wavelengths found an expanding one-sided relativistic jet ($v \sim 0.81c$,), with an inclination to the line-of-sight of $\lesssim 14^\circ$ [39, 55]. High-energy γ-rays (HE γ-rays : > 100 MeV) from Cyg X-3 have been firmly detected by the new generation of space telescopes. AGILE found evidence of transient γ-ray activity from Cyg X-3 in 2009 [54] as confirmed by the *Fermi*-LAT detections [23]. Furthermore, *Fermi*-LAT could determine also the orbital modulation of the γ-ray emission [23]. The photon spectrum (between 100 MeV and 3 GeV) detected by AGILE during the peak flaring activity is well-fitted by a power law with a photon index $\Gamma = 2.0 \pm 0.2$. On the other hand, the average spectrum above 100 MeV measured by *Fermi*-LAT for two active windows (of about two months each) gives $\Gamma = 2.70 \pm 0.25$. This difference could indicate a fast spectral hardening of the high-energy emission during the short and intense γ-ray events (lasting $\sim$1-2 days) detected by AGILE. Nevertheless, the peak γ-ray luminosity detected above 100 MeV by both AGILE and *Fermi*-LAT corresponds to $L_\gamma \approx 10^{36}$ erg s^{-1}. These observations provide direct evidence that extreme particle acceleration occurs in Cyg X-3 in a transient fashion, most likely associated with the relativistic jet ejection and/or propagation. Both AGILE [54, 16, 43] and Fermi [23, 19] found the same multi-frequency conditions for the γ-ray activity. In particular, [43] found that the transient γ-ray emission

detected by AGILE is associated with very faint hard X-ray activity[1] and generally occurs a few days before intense major radio flares. The γ-ray transient emission is observed when the system is moving into or out of the quenched state, a characteristic state of Cyg X-3 that generally precedes a major radio flare. The quenched state, which has been found to be a key trigger condition for the γ-ray activity, is characterized by a very low or undetectable level of radio flux density and a bright soft X-ray emission with a particular X-ray spectrum (the hypersoft spectrum, 35).

At very high energies (VHE γ-rays : > 250 GeV), Cyg X-3 was observed by the MAGIC telescope for about 70 hr between 2006, March and 2009, August. These observations correspond to different X-ray/radio spectral states, and also show periods of enhanced γ-ray emission [8]. No TeV γ-rays from Cyg X-3 have been detected and upper limits on the integrated γ-ray flux above 250 GeV are 2.2×10^{-12} photons cm^{-2} s^{-1}[8]. We notice that the lack of evidence for detectable TeV emission from Cyg X-3 can be due to the strong absorption of these photons (through $\gamma\gamma$ absorption on ultraviolet (UV) stellar photons from the WR star) or due to limited time of observation. If γ-ray emission from Cyg X-3 is caused by hadronic interactions, our knowledge about the source would be greatly improved by the detection of HE neutrinos. For proton-proton (pp) interactions, the emitted photons and neutrinos can have comparable intensities. In this case, high-energy photons can be absorbed and neutrinos can freely escape from the source. Neutrinos carry invaluable information about the existence (or absence) of energetic protons and shed light on the location of the γ-ray production region.

Recently, the IceCube collaboration reported on searches for neutrino sources at energies above 200 GeV in the Northern sky of the Galactic plane (including Cyg X-3), using the data collected by the South Pole neutrino telescope, IceCube, and AMANDA [30]. Interestingly, it turns out that during this period Cyg X-3 was observed both close to γ-ray flaring activity as well as in different X-ray/radio states. A maximum likelihood test using a time-dependent version of the unbinned likelihood ratio method was applied to the IceCube data. As a result, no evidence for a signal was found in the neutrino sample. The 90% confidence level upper limits on the differential muon neutrino flux from Cyg X-3 for E^{-2} and E^{-3} spectra are: dN/dE $\leq$ 0.7×10^{-11} TeV^{-1}cm^{-2}s^{-1} and dN/dE $\leq 5 \times 10^{-11}$ TeV^{-1}cm^{-2}s^{-1}, respectively [30].

Here we focus on the hadronic scenario for high energy emission from the microquasar Cyg X-3 . We assume that the jet of Cyg X-3 accelerates both leptons and hadrons to high energies. The accelerated protons escape from the jet and, interacting with hadronic matter of the WR star, produce γ-rays and

[1]The γ-ray activity has been detected – always during soft X-ray spectral states – when the 15-50 keV count rate detected by *Swift*/BAT (Burst Alert Telescope) was lower than 0.02 counts cm^{-2} s^{-1} ($\approx$ 0.091 Crab).

neutrinos. By normalizing our model with the γ-ray emission of Cyg X-3 at its peak (using AGILE data) and considering the MAGIC upper limits (that we interpret in terms of a strong $\gamma\gamma$ absorption on the stellar photons), the corresponding flux of HE neutrinos is calculated and compared with the IceCube sensitivity.

4.2 The model

The origin of HE γ-rays from microquasars can be interpreted within both leptonic and hadronic scenarios. The jet in the microquasars is a powerful particle accelerator (electrons and/or protons), and the photon field and/or wind from companion star can be a target for γ-ray production. In the leptonic scenario, HE γ-rays are produced from inverse Compton (IC) scattering of soft seed photons (from the companion star and from the accretion disk) by energetic electrons. In the case of Cyg X-3 , the leptonic scenario has been extensively discussed in the literature [21, 59, 43]. In particular, 43 applied this picture to the AGILE observations of Cyg X-3 in flaring states, showing how a leptonic scenario can explain the spectral shape at GeV energies as well as the hard X-ray emission at $\sim$100 keV observed during the transient γ-ray activity.

By considering a hadronic picture, since protons are characterized by a longer cooling time than electrons, we can assume that protons are accelerated well above 10 TeV. The detection of a periodic TeV γ-ray signal (which could be evidence for production of TeV photons in a binary system) would provide additional information on the problem of distinguishing leptonic and hadronic contributions. If accelerated in the presence of a strong cooling photon background, electrons would possibly produce VHE γ-rays by IC scattering. On the other hand, hadrons would produce VHE γ-rays by interaction of a suitable gaseous target. After escaping from the jet, protons can interact both with the X-ray photon field from the accretion disk ($p\gamma$ interaction) as well as with the hadronic component of the stellar wind (pp interaction). In both cases, a significant flux of TeV γ-rays and neutrinos are predicted: while the γ-rays are absorbed (depending on the energy), the neutrinos escape from the region with negligible absorption. The emerging flux of HE neutrinos can significantly exceed the γ-ray observed flux (approximately $\exp(\tau)$ times higher, where τ is the optical depth of $\gamma\gamma$ absorption). For example in the case of the microquasar LS 5039, the flux of HE neutrinos can be as large as 1.6×10^{-11} cm^{-2} s^{-1} (for energy greater than 1 TeV), above the sensitivity threshold of experiments in the Mediterranean Sea [4]. Therefore the binary systems could have a high flux of HE neutrinos, which can be detected by the current generation of detectors.

Hadronic models based on $p\gamma$ interactions require acceleration of protons in the inner jet up to the energies of 10^{16} eV in order to produce a signifi-

cant flux of HE γ-rays and neutrinos. On the other hand, models based on pp interactions can explain the observed γ-ray flux by requiring lower energies of accelerated protons. Production of HE neutrinos from $p\gamma$ interaction in Cyg X-3 have been discussed in [13]: the expected number of neutrinos – assuming the IceCube sensitivity – during 61 days is 0.02, corresponding to a non-detectable flux. An alternative hadronic scenario for production of γ-rays from Cyg X-3 was discussed in 43, within the jet-wind interaction model. They found that the constraints on the energetics of the system are physically reasonable: the required jet kinetic power is lower than the Eddington accretion limit for the source, and the resulting spectral shape is consistent with the observed spectrum above 100 MeV. In our model we assume that the energy budget in the jet is dominated by the kinetic energy of an *e-p* plasma and it contains a significant population of protons. These particles are accelerated along the jet propagation (e.g via shock acceleration) and can reach very high energies; in the binary frame this energy is even higher (multiplied by the Lorentz factor of the jet). Due to the slowly cooling of the protons in the jet, their maximum energy will be likely limited by the size of acceleration region: the Larmor radius (r_L) of the protons should be contained in the acceleration region $r_L \leq R_{jet}$ where R_{jet} is the jet radius and $r_L = E_m/eB$, where e is the elementary charge. Depending on the efficiency of acceleration, the magnetic field (B), and the jet radius (R_{jet}), the proton maximum energy (E_m) can be as large as 100 TeV. However, the accelerated protons can escape from the jet at some distance from the compact object since the magnetic field gets weaker. In case this occurs in a binary system, the protons interact with the dense wind of the WR star, producing neutral and charged pions via inelastic hadronic scattering. The neutral pions subsequently decay in γ-rays , while muon and electron neutrinos (ν_μ, ν_e) are produced by the decays of $\pi^\pm$ (e.g., $\pi^+ \rightarrow \mu^+ + \nu_\mu \rightarrow e^+ + \nu_e + \nu_\mu + \bar{\nu}_\mu$). If we define L_p as the luminosity of relativistic protons, the corresponding luminosity of γ-rays is $L_\gamma \approx c_{pp}\, L_p$ where c_{pp} is the energy transfer efficiency from relativistic protons to secondary particles (for simplicity it is assumed that the escape time of protons from the binary system is longer than the cooling time). Similarly, expressing the acceleration power of protons in terms of the total jet power, $L_p \approx \zeta\, L_{jet}$, one finds the following relation between jet power and γ-ray luminosity, $L_\gamma \approx \zeta c_{pp}\, L_{jet} = \xi L_{jet}$, where ζ is the acceleration efficiency and $\xi = \zeta c_{pp}$ is the efficiency of γ-ray production. Assuming $c_{pp} \approx \zeta \approx 10\%$ ($\xi \approx 10^{-2}$), and a peak γ-ray isotropic luminosity above 100 MeV of $L_\gamma \sim 10^{36}$ erg s^{-1}, the corresponding jet power is $L_{jet} \sim 10^{38}$ erg s^{-1}, which is an order of magnitude lower than the Eddington accretion limit for the system (assuming that the compact object in Cyg X-3 is a black hole with a mass of $M_x = 10\ M_\odot$, where $M_\odot$ is the solar mass) and it is consistent with the average bolometric luminosity of the hypersoft state, $L_{bol}^{HYS} \approx 1.2 \times 10^{38}$ erg s^{-1} [35]. Furthermore, as demonstrated by [17], it is unlikely that the HE γ-rays have a

coronal origin (unless the corona is unrealistically extended): the observed γ-ray emission is linked to the physics of the jet and created outside the γ-ray photosphere (at distances greater than 10^8-10^{10} cm from the compact object).

Fermi-LAT observations of the source revealed a γ-ray orbital modulation [23] coherent with the orbital period ($t_{mod} = 4.8$ hr). The folded emission above 100 MeV is characterized by a sharp maximum in correspondence to the superior conjunction of the system (compact object behind the WR star, with respect to the line of sight). The γ-rays appear to be approximately in antiphase with the X-ray modulation, a fact that may be linked to the different physical origin of the two components. The modulated γ-rays are produced only if the protons are confined in the binary system in time scales less than $\xi\, t_{mod}$ otherwise the protons will escape from the binary system. Since the cooling time for pp interactions is $t_{pp} \approx 10^{15}/N$ s ($N = n_H/1\,\mathrm{cm}^{-3}$), from the relation $t_{pp} = \xi\, t_{mod}$, the condition for γ-ray modulation is satisfied only for densities (n_H) larger than $\approx 6 \times 10^{12}$ cm^{-3} (assuming $\xi \approx 10^{-2}$ and $t_{mod} = 4.8$h). Accordingly, this condition is satisfied especially near superior conjunction because of an increase of the density along the orbit (anisotropic wind) or due to protons interacting with clumps (regions where the density is significantly higher than average value) [10]. At other phases along the orbit, the density of the wind should be significantly lower and since this change of density causes the change of luminosity of produced γ-rays , this results a modulation of γ-ray signal.

4.3 Production and absorption of gamma-rays.

In the binary systems the production of γ-rays (both in leptonic and hadronic origin) is accompanied by strong absorption of these photons. Depending on both their energy and the site of HE production, the emitted γ-rays can be absorbed by interactions with the X-ray photons from the corona/disk complex or with the UV photon field from the companion star. We discuss below the production of γ-rays from pp interaction as well as the opacity of photon absorption.

4.3.1 Production of gamma-rays and neutrinos from pp interaction

Hadronic inelastic scattering, between high-energy protons (accelerated in the jet) with cold protons from the WR wind, is responsible for the production of secondary γ-rays and neutrinos. The fluxes of produced particles are calculated using the analytical approximation derived in [34], obtained from numerical simulations of pp interaction with the publicly available code SIBYLL. The analytical formulae provide a very good description of the flux

and energy distribution of secondaries for energies above 100 GeV. The formula for γ-rays also includes the contribution of η meson decay, in addition to that of π^0, with an overall accuracy of order a few percent.
At energies below 0.1 TeV and down to the rest energy of the π-meson, the fluxes of γ-rays and neutrinos are modeled with delta function approximation as suggested by [34], namely the fluxes are given by:

$$\Phi_i(E_i) = \frac{c\, A_i\, \kappa\, n_H}{4\pi\, D^2\, K_\pi} \int_{E_{\pi,\mathrm{th}}}^{\infty} \frac{\sigma_{pp}(E_c)\, N_p(E_c)}{\sqrt{E_\pi^2 - m_\pi^2 c^4}} \mathrm{d}E_\pi \tag{4.3.1}$$

for both particle type i ($i = \gamma, \nu$), $E_{\pi,\mathrm{th}} = \frac{E_i}{1-r_i} + (1-r_i)\frac{m_\pi^2 c^4}{4\,E_i}$ where $r_\gamma = 0$, $r_\nu = (m_\mu/m_\pi)^2$, $A_\gamma = 2$, and $A_\nu = (1-r_\nu)^{-1}$. In Eq. (4.3.1) K_π is the mean fraction of proton kinetic energy transferred to pions, c is the speed of light in a vacuum, D is the distance from the source, κ is the free parameter to match the results of Monte-Carlo simulations [34], σ_{pp} is the pp inelastic interaction cross section, $E_c = m_p c^2 + E_\pi/K_\pi$ and m_p, m_μ, m_π are the proton, muon and pion masses, respectively.

4.3.2 Absorption of gamma-rays

The produced γ-rays can be absorbed by interactions with UV stellar photons from the companion star. In the calculations below, we take into account this absorption by using the opacity averaged over the injection angles:

$$\tau_\gamma(E_\gamma, r) = \int_r^\infty \int_{\epsilon_{min}}^\infty n(\epsilon_0,\, r')\sigma_{\gamma\gamma}(\epsilon_0, E_\gamma)\mathrm{d}\epsilon_0\, \mathrm{d}r', \tag{4.3.2}$$

where ϵ_0 is energy of the companion star's photons, ϵ_{min} is the threshold of pair production, $\epsilon_{min} = m_e^2 c^4/E_\gamma$, E_γ is the energy of the γ-ray , $m_e c^2$ is the electron rest energy and $\sigma_{\gamma\gamma}(\epsilon_0, E_\gamma)$ is the cross section for photon-photon pair production [26]. The distribution of stellar photons is assumed to have a blackbody spectrum peaking at the star's effective temperature (T_{eff}):

$$n(\epsilon_0, r) = \frac{2\pi\epsilon_0^2}{(h\,c)^3} \frac{1}{e^{\epsilon_0/k\,T_{\mathrm{eff}}} - 1} \frac{R_\star^2}{r^2}, \tag{4.3.3}$$

where h and k are the Planck and Boltzmann constants respectively, and $R_\star$ is the radius of the companion star. For Cyg X-3 we adopt the following values: $T_{\mathrm{eff}} = 10^5$ K, and $R_\star = 6 \times 10^{10}$ cm.

This absorption depends strongly on the geometry. It depends on the relative location of the γ-ray source, the companion star, and the line of sight to the observer. We calculated the opacity, which depends on the distance from the companion star (r), by averaging over the injection angles. This is illustrated in Fig. 4.1 where the opacity is calculated from Eq. 4.3.2 for $r = R_\star$,

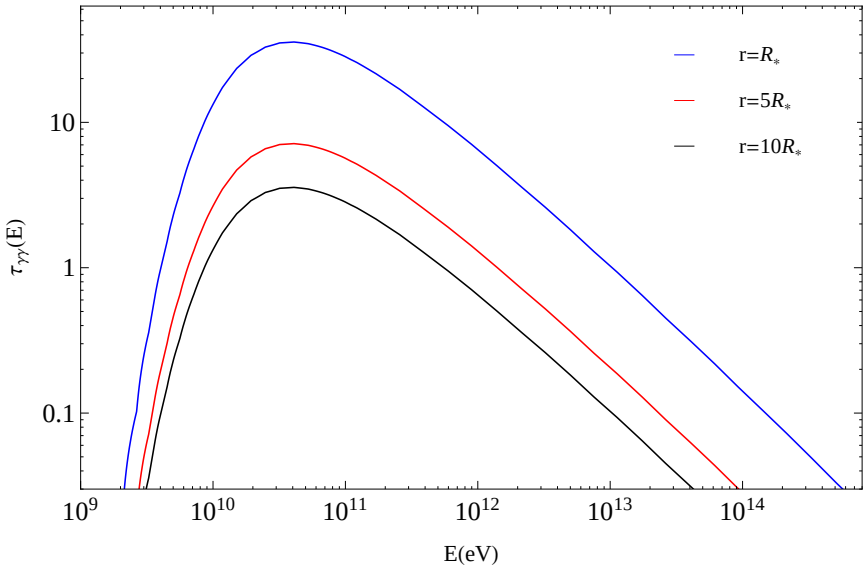

Figure 4.1: The opacity of photon-photon pair production (averaged over injection angles) calculated for different distance from the companion star for the Cyg X-3 system

.

$5R_\star$ and $10R_\star$. The VHE γ-rays produced very close to star (e.g. $r = R_\star$) will be heavily attenuated ($\tau_{\gamma\gamma} \approx 30$ for $E_\gamma = 100\,\mathrm{GeV}$), and the observed spectrum of VHE photons would be hardened compared to its intrinsic shape. However this opacity will vary depending on the distance, for comparison, the opacity of gamma-photon interaction at distance $10R_\star$ is $\tau_{\gamma\gamma} \approx 3.0$ (at 100 GeV). It rapidly drops for higher energies, and the source becomes transparent for γ-rays above 10 TeV. It should be noted that a similar study of pair-production opacity along the orbit presented by [59] found consistent results: the opacity peaks around 100 GeV and drops at higher energies.

4.4 The results

In our model we assume that the energy distribution of accelerated protons follows a power law plus a high-energy cut-off at 100 TeV:

$$N_p(E_p) \sim E_p^{-\alpha} \exp\left(-\frac{E_p}{100\,\mathrm{TeV}}\right). \tag{4.4.1}$$

Using the proton distribution given by Eq. (4.4.1), the corresponding fluxes of HE γ-ray and neutrinos are calculated. In our calculations, we focus on ν_μ and $\bar{\nu}_\mu$ for which neutrino detectors are most sensitive.

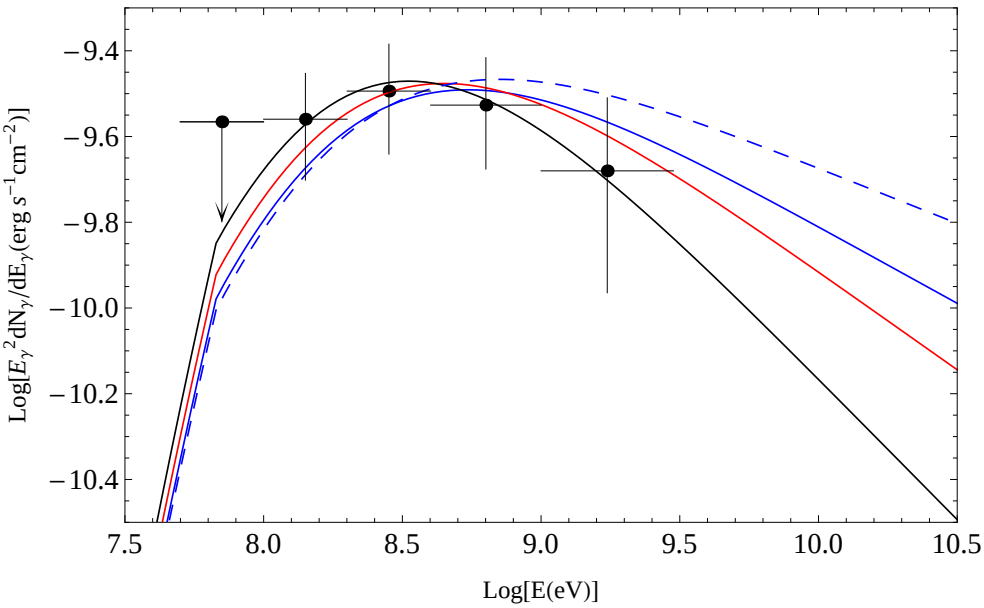

Figure 4.2: Hadronic modeling of the γ-ray flaring spectrum detected by AGILE assuming different indices of the initial proton energy distribution. The blue, red and black solid lines correspond to power-law indices $\alpha = 2.4$, 2.5 and 2.7, respectively; the dashed line corresponds to $\alpha = 2.3$.

As discussed in the previous section, γ-rays produced from pp interaction will be effectively absorbed by stellar photon field and this absorption amplitude depends on the distance from the star where these photons are created. Accordingly, below we discuss different possibilities for the γ-ray absorption in Cyg X-3 , assuming that gamma-photon interactions occur close (strong absorption) or far away from the companion star (weak absorption).
At the same time, since the cross section of $\gamma\gamma$ interaction achieves its maximum at $\epsilon E/(m_e c^2)^2 \approx 4$, the absorption of GeV γ-rays will be effectively in the X-ray photon field. However, since in our model the γ-rays are produced farther from the compact object, where the density of X-ray photon field is low, these photons escape the region without significant absorbtion. Accordingly, using the AGILE observations of Cyg X-3 γ-ray flares, the limit on the power-law index of proton energy distribution can be derived. The resultant fits of the data for different initial proton energy distributions are shown in Fig. 5.2.1. As one can see, the minimum power-law index which can reproduce the observed data corresponds to $\alpha = 2.4$ (blue solid line), since for lower power-law indices predicted flux of γ-rays is larger than the γ-ray data (blue dashed line in Fig. 5.2.1). Moreover, softer proton spectra fit better the data (see the red and black lines in Fig. 5.2.1, calculated for α = 2.5 and 2.7 respectively).

Fig. 4.3 (a) shows the γ-ray fluxes calculated for the proton energy distributions given by Eq. 4.4.1 with $\alpha = 2.4$, 2.5 and 2.7 (blue, red and black colors

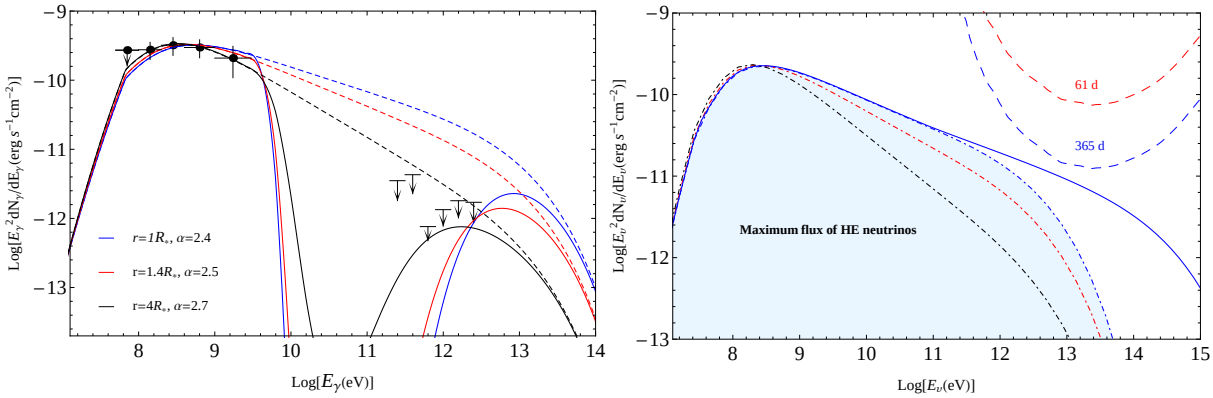

(a) (b)

Figure 4.3: Panel (a): Calculated γ-ray unabsorbed (dashed lines) and absorbed (solid lines) emission shown with the γ-ray flaring flux ($\sim$8 days) detected by AGILE [43], and the MAGIC upper limits obtained when Cyg X-3 was in the soft state (four observation cycles, corresponding to a total of 30.8 hours, 8). The γ-ray absorption by UV stellar photons is calculated for different distances r from the companion star. In panel (b) the corresponding calculated spectrum of HE neutrinos is presented, the filled area represents the maximum flux of HE neutrinos. In panel (b) the solid blue line corresponds to a neutrino model with the same parameters of the blue dot-dashed curve ($r = R_\star$, $\alpha = 2.4$), but with a maximum energy of protons of 10 PeV. Red and blue dashed lines in panel (b) corresponds to IceCube sensitivities expected for two-month (61 days) and one-year (365 days) exposure time, respectively.

respectively). The dashed lines corresponds to the unabsorbed flux of γ-rays , instead the corresponding absorbed spectra are depicted with solid lines. As one can see, in all cases the predicted unabsorbed flux of γ-rays at TeV energies is larger than the ULs derived from MAGIC observations. However, taking into account the absorption of γ-rays , our model is in agreement with the observed data in MeV/GeV and TeV energies. For example, in the case of a proton index of $\alpha = 2.4$ (which is related to the highest γ-ray flux), assuming that the γ-rays are produced at the distance $r = R_\star$, the density of stellar photon field is so high that the absorbed γ-ray spectrum is lower than the MAGIC ULs (blue solid line in Fig. 4.3 (a)). Similar results are obtained for values of $\alpha = 2.5$ with $r = 1.4R_\star$ (red line in Fig. 4.3 (a)), and for $\alpha = 2.7$ with $r = 4R_\star$ (blue line in Fig. 4.3 (a)). We remark that the values presented here corresponds to the maximum distances from the star where the γ-rays can be created: for closer distances, the absorption is higher and the predicted flux will be smaller.
Neutrinos are produced together with the γ-rays , but unlike the γ-rays they escape from the region without any absorption. In Fig. 4.3 (b) we show the

resulting neutrino fluxes from Cyg X-3 corresponding to the γ-ray models of Fig. 4.3 (a). Since the minimum power-law index obtained from the γ-ray observations corresponds to $\alpha = 2.4$, the predicted flux of neutrinos can be considered as a maximum flux during the γ-ray activity of the microquasar (this is shown with a filled area in Fig. 4.3 (b)). This predicted flux of HE neutrinos is compared with the IceCube sensitivities expected for different exposure times: two-month (61 days) and one-year (365 days) exposure time (red and blue dashed lines in Fig. 4.3 (b), respectively). The effective area for the 40-string configuration [1] have been scaled to the 86-string configuration[2] (full string configuration). The maximum predicted flux of neutrinos is almost two order of magnitude less than the 61 day IceCube sensitivity, in agreement with the absence of a detectable neutrino signal from Cyg X-3 from the current IceCube observations [30]. Nevertheless, we can assume that relativistic particles inside the jet can be accelerated far above 100 TeV, reaching PeV energies (supposing that Cyg X-3 is a Galactic "Pevatron"). Accordingly, if the cut-off energy in the proton spectrum (see Eq. 4.4.1) is at 10 PeV, the predicted flux of HE neutrinos is slightly lower than the IceCube sensitivity for one-year exposure time (solid blue line in Fig. 4.3 (b)). Therefore, future detection of HE neutrinos from Cyg X-3 is possible if the particles in the jet are accelerated up to ultra high energies.

In the previous discussion only the γ-ray data from AGILE observations are used. However, the derived conclusions are valid also for the γ-ray spectrum obtained by *Fermi*-LAT during a prolonged γ-ray activity of the microquasar [23]. The predicted flux of HE neutrinos, related to the γ-ray activity detected by *Fermi*-LAT , will be slightly lower than the ones presented in Fig. 4.3 (b), since the *Fermi*-LAT photon index for the average emission from Cyg X-3 above 100 MeV is $\Gamma = 2.7$ [23], instead of the value $\Gamma = 2.0$ determined by AGILE in the range 100 MeV - 1 GeV.

4.5 Discussion

Hadronic γ-ray emission from Cyg X-3 , discussed and presented in the previous sections, requires an effective acceleration of hadrons (protons) in the jet of the microquasar. The total energy of the protons (for $\alpha = 2.4$) corresponds to $W_p \approx 1.74 \times 10^{40}$ erg, assuming the number density of the wind to be $n_H = 6 \times 10^{12}$ cm^{-3}. The kinetic power of protons in the jet ($L_p = W_{pp}/t_{pp}$) would be $L_p = 1.04 \times 10^{38}$ erg s^{-1}, consistent with the hypersoft state bolometric luminosity. This flux of γ-rays would be accompanied by the flux of HE neutrinos and, for a proton injection power $L_p = 1.04 \times 10^{38}$ erg s^{-1}, the predicted neutrino flux is $f_{10\,TeV} \approx 9.1 \times 10^{-12}$ erg cm^{-2} s^{-1}

[2]The real effective area related to the 86-string IceCube configuration for a point source may be marginally different, but so far no public data are available.

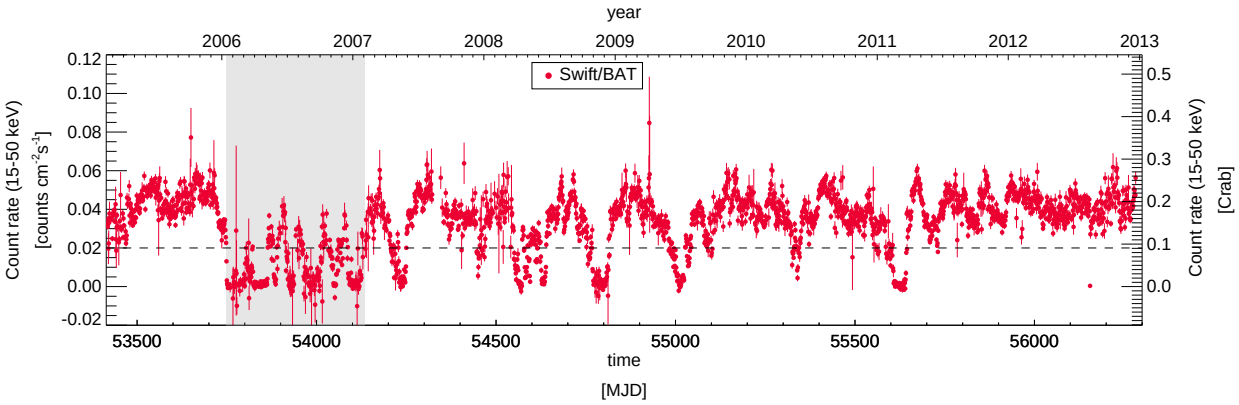

Figure 4.4: Hard X-ray light curve of Cyg X-3 as detected by *Swift*/BAT (15-50 keV) between February 2005 and January 2013. The horizontal dashed line represents the transition level (0.02 counts $\mathrm{cm}^{-2}\,\mathrm{s}^{-1} \approx 0.091$ Crab) between soft and hard X-ray spectral state. Gamma-ray emission above 100 MeV is expected during minima of the hard X-ray curve [43].

at 10 TeV (solid line in Fig. 4.3 (b)). Furthermore, the minimum detectable neutrino flux for a neutrino point source with a generic E^{-2} spectrum, after one year of operation, is $f_{sens} = 2.72 \times 10^{-11}\,\mathrm{erg\,cm^{-2}\,s^{-1}}$ at 5 σ significance [7]. We then obtain $f_{10\,\mathrm{TeV}}/f_{sens} \approx 0.3$. This estimate shows that only a quite hard proton injection rate (of index $\alpha < 2.4$) extending up to 10 PeV can produce a detectable flux of HE neutrinos from Cyg X-3 . The flux of HE neutrinos depends, not only on the proton injection rate (which may be time variable), but also on the duration of the HE activity of the source. It is known that the microquasar Cyg X-3 emits γ-rays only in specific X-ray conditions: namely, during bright soft X-ray spectral states coincident with *minima* of the hard X-ray light curve [54, 23, 19, 43]. In principle, these states could last several months [23] or even longer, with a strong probability of emitting γ-rays . These prolonged episodes of minimal hard X-ray emission (and corresponding maximal soft X-ray emission) might imply a significant increase of neutrino emission which can be detected by IceCube under favorable conditions. Interestingly, the hard X-ray light curve as detected by *Swift*/BAT (15-50 keV) (see Fig. 4.4) shows such a prolonged activity. Namely, with the gray region of the plot is indicated a prolonged period (MJD: ∼53749–54136, between 2006 and February 2007) in which Cyg X-3 is found to be most of the time (∼70%) in a soft state (*Swift*/BAT count rate $\lesssim$ 0.02 counts $\mathrm{cm}^{-2}\,\mathrm{s}^{-1}$). Therefore, if the conditions for γ-ray emission discussed by 43 are valid, we deduce that in that period Cyg X-3 was characterized by a quasi-continuous emission of γ-rays and possibly detectable neutrinos. Unfortunately neither AGILE nor *Fermi* (nor sensitive neutrino detectors) were operational in 2006 to test this picture. In the future, such a possible prolonged active state accompanied

by a quasi-continuous emission of γ-rays (of hadronic origin) might reach a neutrino flux close to detection by instruments such as IceCube.

4.6 Conclusions

Effective particle acceleration in microquasar jet makes these objects strong sources of MeV-TeV γ-rays . These γ-rays can be produced via leptonc interactions (e.g. IC scattering of low energy photons by relativistic electrons), as well as via hadronic processes (e.g., $p\gamma$ or pp interactions). In case of hadronic interactions, the flux of γ-rays is accompanied by emission of HE neutrinos. Therefore, these sources are interesting target of observations with HE neutrino detectors.

Here we investigated the possibility of detecting HE neutrinos from Cyg X-3 within a hadronic model of emission. We discussed a simplified picture of hadronic γ-ray production, namely we assumed that the protons are effectively accelerated by the jet up to 100 TeV energies (the achieved maximum energy of protons depends on the magnetic field and on the size of jet). These protons can escape from the jet and interact with cold protons in the wind of the companion star. From these inelastic collisions, neutral and charged pions are produced with subsequent substantial neutrino emission. In this scenario, the effective production of γ-rays occurs only if the surrounding matter (number) density is larger than $\approx 6 \times 10^{12}$ cm^{-3} (corresponding to a cooling time $\leq \xi\, t_{mod}$, with $\xi \approx 10^{-2}$). This condition is expected to be satisfied for Cyg X-3 at superior conjunction where the modulated γ-ray emission along the orbit reaches its maximum [23]. The absorption of γ-rays (by UV stellar photons from the WR star) does not affect the propagation of photons at MeV/GeV energies (unlike the TeV γ-rays), therefore the minimum index of the initial proton energy distribution can be derived from the Cyg X-3 γ-ray flares to be $\alpha \geq 2.4$ (from AGILE data). The spectrum of γ-rays and high-energy neutrinos can be then calculated. Taking into account the absorption of TeV γ-rays as deduced from the MAGIC upper limits, we can constrain the distance from the companion star where the γ-rays should be created. Within this distance, the absorption modifies the spectrum at TeV energies. The injection rate of protons should be $L_p \approx 10^{38}\,\mathrm{erg\,s^{-1}}$ in order to explain the observed spectrum of γ-rays . The required power is physically reasonable: it is consistent with the bolometric luminosity during the hypersoft spectral state (correlated to the γ-ray transient activity, 43), and it is lower than the Eddington accretion limit for a stellar black hole mass in Cyg X-3 . Together with γ-rays , HE neutrinos are produced, escaping the region without any absorption. We found that a maximal neutrino flux (expected during the γ-ray activity of Cyg X-3) corresponds to an accelerated proton distribution with $\alpha = 2.4$. In case of short exposure time (two months), the predicted flux of HE neutrinos is almost two orders of magnitude less than the 61-day IceCube sensitivity. Only assuming that protons are accelerated up to 10 PeV energies with a spectrum harder than $\alpha = 2.4$, the predicted neutrino flux would be detectable by the IceCube full-string sensitivity (with 1-year exposure time). Whether a proton spectrum harder than $\alpha = 2.4$ can be produced in Cyg X-3

in a time variable fashion not to contradict TeV upper limits is an open question that will be investigated by future observations. Long term observations of Cyg X-3 with IceCube combined with GeV and TeV observations can give important information about emission of neutrinos from microquasars, providing invaluable constraints on the hadronic particle density in relativistic jets. These considerations show how Cyg X-3 is a crucially interesting source, not only for radio-to-γ-ray observations, but also for new-generation neutrino detectors.

5 On the gamma-ray emission from the core and radio lobes of the radio galaxy Centaurus A

5.1 Introduction

The bright, nearby radio galaxy Cen A is the best-studied extragalactic objects over a wide range of frequencies [32]. Its unique proximity (d$\sim$3.7 Mpc) and peculiar morphology allow a detailed investigation of the non-thermal acceleration and radiation processes occurring in its active nucleus and its relativistic outflows.
At MeV energies, Cen A has been observed with both OSSE (0.05-4 MeV) and COMPTEL (0.75-30 MeV) onboard the Compton Gamma-Ray Observatory (CGRO) in the period 1991-1995 [50]. An agreement of the OSSE spectrum with the COMPTEL one in the transition region around 1 MeV, and correlated variability has been found [50]. At higher energies, a marginal (3σ) detection of gamma-rays from the core of Cen A was reported with EGRET (0.1-1.0 GeV), but due its large angular resolution the association with the core remained rather uncertain [29]. Unlike the initial variability (month-type?) seen at lower energies, the flux detected by EGRET appeared stable during the whole period of CGRO observation [48]. At high-energy (HE; 200 MeV$<$ E $<$ 100 GeV) Fermi-LAT has recently detected γ-ray emission from the core (i.e., within $\sim 0.1^{\circ}$) and the giant radio lobes of Cen A ([2, 3]): An analysis of the available ten-month data set reveals a point-like emission region coincident with the position of the radio core of Cen A, and two large extended emission regions detected with a significance of 5 and 8σ for the northern and the southern lobe, respectively. The HE emission from the core extends up to $\sim$ 10 GeV and is well described by a power-law function with photon index $\sim$ 2.7. At VHE ($>$ 100 GeV) energies, Cen A has also been detected (with a significance of 5σ) by the H.E.S.S. array based on observations in 2004-2008. The results show an average VHE spectrum compatible with a power law of photon index $\Gamma = 2.73 \pm 0.45_{stat} \pm 0.2_{syst}$ and an integral flux $F(E > 250\,\mathrm{GeV}) = (1.56 \pm 0.67_{\mathrm{stat}}) \times 10^{-12}\,\mathrm{cm}^{-2}\,\mathrm{s}^{-1}$[5]. No evidence for variability has been found in the H.E.S.S. data set, but given the weak signal no certain conclusions can be drawn.
i) In the case of the core the apparent lack of significant variability features at

GeV and TeV energies has so far precluded robust inferences as to the physical origin of the core emission in Cen A. Unfortunately, the resolutions of current gamma-ray instruments is not sufficient to localize the gamma-ray emitting region(s) either: The angular resolutions of both the H.E.S.S. array ($\sim 0.1^\circ$) and *Fermi* (0.1° -1°, depending on energy) correspond to linear sizes of the gamma-ray emitting region(s) of about 5 kpc or larger. This $\sim$ 5-kpc-region contains several potential gamma-ray emitting sites such as the central black hole, the sub-pc- or the kpc-scale jet etc. Based on the reported results, one thus cannot distinguish whether the gamma-rays observed from the core in Cen A originate in compact or extended regions. This motivated us to have a new look on the core emission based on four year of *Fermi* data.
ii) If the extended HE emission from Cen A is generated by indeed inverse-Compton up-scattering of CMB and EBL (extragalactic background light) photons, this could offer a unique possibility to spatially map the underlying relativistic electron distribution in this source. The detection of GeV γ-rays from the radio lobes implies magnetic field strengths $\lesssim 1$ μG (e.g., [2]). This estimate can be obtained quite straightforwardly from the comparison of radio and γ-rays, assuming that these radiation components are produced in the same region by the same population of electrons through synchrotron and inverse-Compton processes. In general, however, the radio and the γ-ray region do not need to coincide. While the radio luminosity depends on the product of the relativistic electron density N_e and the magnetic-field square B^2, the inverse-Compton γ-ray luminosity only depends on N_e. This implies that γ-rays can give us model-independent information about both the energy and the spatial distribution of electrons, while the radio image of synchrotron radiation strongly depends on the magnetic field. As a consequence, the γ-ray image can be larger than the radio image if the magnetic field drops at the periphery of the region occupied by electrons. This provides one of the motivations for a deeper study of the extended HE (lobe) emission region in Cen A. We analyze 3 yr of Fermi LAT data, increasing the available observation time by more than a factor of three with respect to the previously reported results. The larger data set allows a detailed investigation of the spectrum and morphology of the lobes with better statistics, especially above 1 GeV, where the spectral shape may reflect cooling effects and/or maximum energy constraints on the parent population of particles generating the HE γ-ray emission.

5.2 The core of Cen A

For the study of HE emission from the core of Cen A we use publicly available *Fermi* $\sim$ 4 yr data from 4th August 2008 to 1st October 2012 (MET 239557417–370742403). *Fermi* on board the Fermi satellite is a pair-conversion telescope designed to detect high-energy γ-rays in the energy range 20 MeV - 300 GeV

[12]. It constantly scans the entire sky every three hours and is always in survey mode although in the past some dedicated pointing observation were done. We use the Pass 7 data and analyze them using the Fermi Science Tools v9r27p1 software package. The entire data set was filtered with *gtselect* and *gtmktime* tools and retained only events belonging to the class 2, as is recommended by the Fermi/LAT science team[1]. To reject atmospheric gamma-rays from the Earth's limb, events with zenith angle < 100 deg are selected. The standard binned maximum likelihood analysis is performed using events in the energy range 0.1–100 GeV extracted from a 10° region centered on the location of Cen A, which is referred to as 'region of interest' (ROI). The fitting model includes diffuse emission components and gamma-ray sources within ROI which are not associated with Cen A (the model file is created based on *Fermi* second catalog [40] and the fluxes and spectral indices are left as free parameters in the analysis. In the model file, the giant radio lobes were modeled using templates from WMAP-k band observation of the source which is extracted from NASA's SkyView. The background was parameterized with the files gal_2yearp7v6_v0.fits and iso_p7v6source.txt and the normalizations of both components were allowed to vary freely during the spectral point fitting.

5.2.1 Spectral Analysis

Initially the continuum gamma-ray emission of the core of Cen A is modeled with a single power law. The normalization and power-law index are considered as free parameters then the binned likelihood analysis is performed. From a binned *gtlike* analysis, the best-fit power-law parameters for the core of Cen A are

$$\left(\frac{dN}{dE}\right)_P = (2.73 \pm 0.12) \times 10^{-9} \left(\frac{E}{100\ \mathrm{MeV}}\right)^{-2.69\pm0.03} . \tag{5.2.1}$$

This corresponds to an integral flux of

$$F_\gamma = (1.61 \pm 0.06) \times 10^{-7}\ \mathrm{photon\,cm^{-2}}s^{-1}, \tag{5.2.2}$$

with only statistical errors taken into account. The test statistic (defined as TS = 2(log L - log L_0), where L and L_0 are the likelihoods when the source is included or not) is TS = 1978 above 100 MeV, corresponding to a $\approx 44\,\sigma$ detection significance. The results are consistent with the parameters found in [3], namely photon index $\Gamma = 2.67 \pm 0.08$ (between 200 MeV and 30 GeV) and integral flux $(1.50 \pm 0.37) \times 10^{-7}$ ph cm^{-2}s^{-1} above 100 MeV (model B). Figure 5.1 shows the spectrum of the core of Cen A obtained by sepa-

[1] http://fermi.gsfc.nasa.gov/ssc/data/analysis/documentation/Cicerone/Cicerone_Data_Exploration/Data_preparation.html

rately running *gtlike* for 12 energy bands, where the dashed line shows the best-fit power-law function for the data given in Eq. (5.2.1). For the highest energy bin (56.2-100 GeV), an upper limit is shown. The spectrum shows a

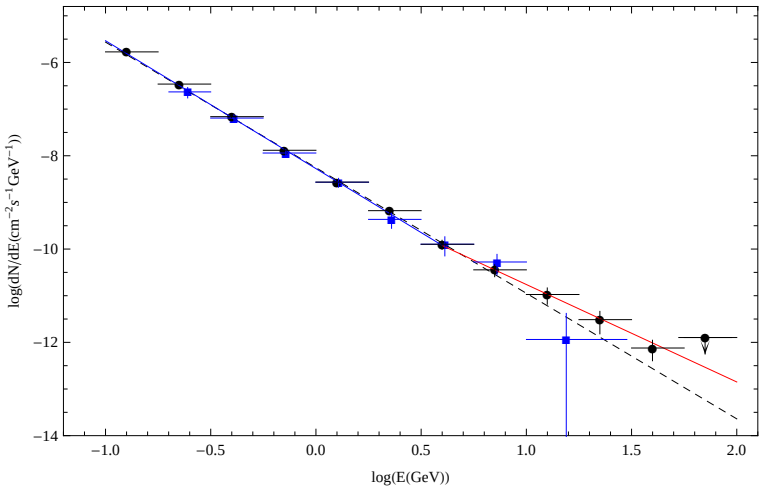

Figure 5.1: Average high-energy gamma-ray (>100 MeV) spectrum of the core of Cen A (black points - this work) as compared to the one based on the initial 10 month data set [blue squares - 3]. The dashed black line shows the power-law function determined from the gtlike. The blue and the red line show power-law fits to the energy bands below and above $E_b \simeq 4$ GeV, respectively.

tendency for a deviation from a single power-law model with respect to the data above several GeV. Indeed, a χ^2 fit of the power-law model to the data gives a relatively poor fit with $\chi^2 = 39.7$ for 9 degrees of freedom (dof), and its probability is $P(\chi^2) < 2 \times 10^{-5}$. In order to investigate this in more detail, the core spectrum is modeled with a broken power-law model and *gtlike* tool is retried. The best-fit broken power-law parameters are

$$\left(\frac{dN}{dE}\right)_{BP} = (1.19 \pm 0.08) \times 10^{-13} \left(\frac{E}{E_b}\right)^{-\Gamma_{1,2}}, \tag{5.2.3}$$

and

$$F_\gamma = (1.67 \pm 0.06) \times 10^{-7} \,\text{photon}\,\text{cm}^{-2}s^{-1}, \tag{5.2.4}$$

with $\Gamma_1 = 2.74 \pm 0.02$ and $\Gamma_2 = 2.12 \pm 0.14$ below and above $E_b = (4.00 \pm 0.09)$ GeV, respectively. In order to compare the power-law and the broken-power-law model, a log likelihood ratio test between the models is applied. The test statistic is twice the difference in these log-likelihoods, which gives 9 for this case. Note that the probability distribution of the test statistic can be approximated by a χ^2 distribution with 2 dof, corresponding to different degrees of freedom between the two functions. The results give $P(\chi^2) = 0.011$, which again indicates a deviation from a simple power-law function. The

results of the data analysis with a broken power-law model reveal a hardening of the (average) gamma-ray core spectrum towards higher energies. The "unusual" break at 4 GeV could most naturally be explained by a superposition of different spectral components. In order to study this deeper, we divide the data set into two parts, i.e., (0.1- 4) GeV and (4-100) GeV. (Note that the 4 GeV-value is obtained from binned maximum likelihood analyses). The core spectrum of Cen A in both energy ranges is then modeled with a power-law function and the *gtlike* tool is separately applied to these two energy bands. The photon index and flux between 100 MeV and 4 GeV are $\Gamma_1 = 2.74 \pm 0.02$ and $F_\gamma = (1.68 \pm 0.04) \times 10^{-7}$ photon cm^{-2}s^{-1}, respectively, and the test statistics gives TS=1944. The result is shown with a blue line in Figure 5.1. On the other hand, for the energy range (4-100) GeV we obtain $\Gamma_2 = 2.09 \pm 0.2$ and $F_\gamma = (4.20 \pm 0.64) \times 10^{-10}$ photon cm^{-2}s^{-1}, respectively, and a TS value of 124.4, corresponding to a $\approx 11\,\sigma$ detection significance. This component is depicted with a red line in Figure 5.1. Moreover, to derive the most likely coordinates of the observed gamma-ray emission *gtfindsrc* tool is applied, yielding RA = 201.387°, Dec = −43.028° with a 95% confidence error circle radius of $r_{95} = 0.04°$and RA = 201.387°, Dec = −43.028° with $r_{95} = 0.04°$for energy ranges (0.1- 4) GeV and (4-100) GeV, respectively. This coordinates are offset by 0.04°and 0.018°from the VLBI radio position of Cen A (RA =201.365°, Dec = −43.019° [38]).

5.3 Temporal Variability

Variability, if present, could provide important constraints on the emitting region(s). An observed HE flux variation on time scale $t_{\rm var}$, for example, would limit the (intrinsic) size of the gamma-ray production region to $R' \leq \frac{\delta_D}{1+z} c t_{\rm var}$ where δ_D is Doppler factor and z is the red-shift. However, previous HE and VHE gamma-ray observations of the core of Cen A with *Fermi* [3] and H.E.S.S. [5] did not find evidence for significant variability. Here we investigate whether the longer (4 yr) data set employed changes this situation. We thus divide the whole data set (from August 4th 2008 to October 1st 2012) into different time bins and generate light curves using the unbinned likelihood analysis with *gtlike*. Due to limited photon statistics the shortest time scale that one can probe is 15 days. In our analysis we generate light curves in 15, 30, 45 and 60 day bins. The normalization of the core and background point sources are treated as free parameters, but the photon indices of all sources and the normalization of the lobes are fixed to the values obtained in 100 MeV-100 GeV energy range for the whole time period. Since no variability is expected for the underlying background diffuse emission, the normalization of both background components is fixed to the values obtained for the whole time period. To search for variability, a χ^2 test was performed. The result for the light curve with 15 day bins is $\chi^2/d.o.f. = 1.22$ and the probability

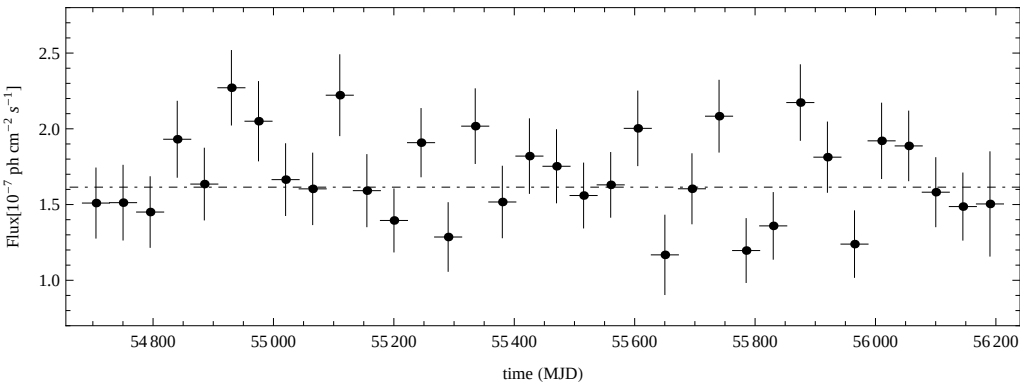

Figure 5.2: Gamma-ray light curve from August 4th 2008 to October 1st 2012. The bin size is 45 day. The background diffuse emission (both galactic and extragalactic) is fixed to the best-fit parameters obtained for the overall time fit. While some variability may be present, limited statistics do not yet allow to make definite conclusions.

is $P(\chi^2) = 0.07$. For the light curves with 30 day and 60 day bins we find $\chi^2/d.o.f. = 1.37$ and $\chi^2/d.o.f. = 1.32$, corresponding to $P(\chi^2) = 0.04$ and $P(\chi^2) = 0.127$, respectively. These results are consistent with no variability. Interestingly however, a similar test for the light curve with 45 day bins gives in $\chi^2/d.o.f. \approx 1.61$ and $P(\chi^2) = 0.015$, indicating a possible variability on 45-day time scale. Unfortunately, because of limited statistics, we cannot make a definite conclusion in this regard. The light curve with 45 day bins is shown in Figure 5.2, with the dot-dashed line indicating the flux from the source for the whole time period (result of likelihood analysis).
In addition, the variability of observed flux above and below 4 GeV is performed. Low detection significance of the component above 4 GeV (TS=124.4) does not allow us to investigate possible variability timescale, whereas for the other component search of variability is performed for 15, 30, 45 and 60 day bins under the same screening conditions described above. So significant variability have been found in any time scale, however still the hints for the variability are present in the lightcurve of 45 day bins $\chi^2/d.o.f. = 1.75$.

5.4 Discussion and Conclusion-1

In the case of high-frequency-peaked BL Lac objects, homogeneous leptonic synchrotron-self-Compton (SSC) jet models often provide reasonable descriptions of their overall spectral energy distributions (SEDs). For Cen A, however, classical one-zone SSC models (under the proviso of modest Doppler beaming) are unable to satisfactorily account for its core SED up to the highest energies [cf. 18, 36, 3]. It seems thus well possible, that an additional component contributes to the observed emission at these energies [e.g., 36, 45].

The results presented here indeed provides support for such a consideration. Our analysis of the 4 yr-data set reveals that the HE core spectrum of Cen A

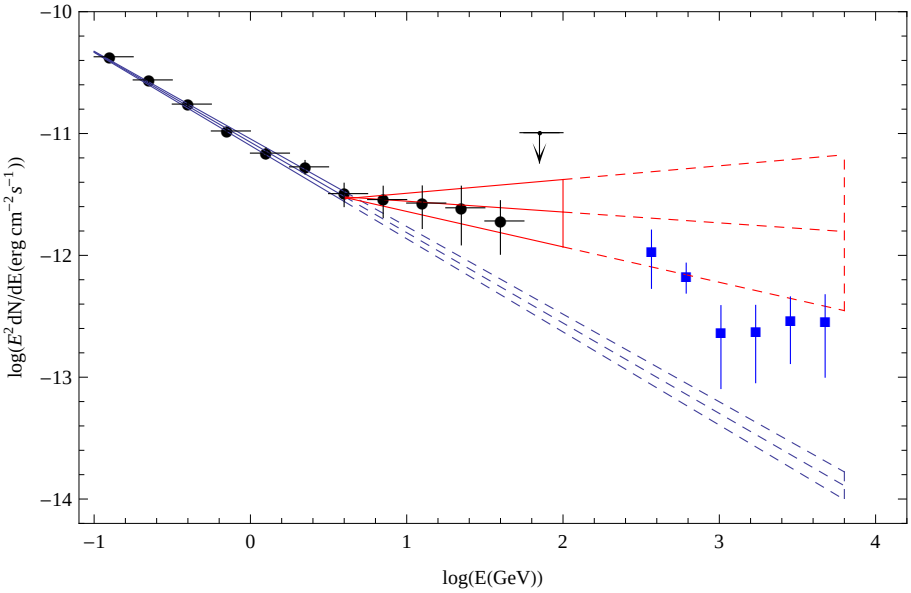

Figure 5.3: Gamma-ray spectrum for the core of Cen A from high (*Fermi* , this work) to very high (H.E.S.S., blue squares) energies. The blue bowtie represents a power-law with photon index 2.74, and the red bowtie a power-law with photon index 2.09. The dashed lines show extrapolations of these models to higher energies. The power-law extrapolation of the low-energy component (blue lines) would under-predict the fluxes observed at TeV energies.

shows a "break" with photon index changing from $\simeq 2.7$ to $\simeq 2.1$ at an energy of $E_b \simeq 4$ GeV. This break is unusual in that the spectrum gets harder instead of softer, while typically the opposite occurs. For a distance of 3.8 Mpc, the detected photon flux $F_\gamma = (1.68 \pm 0.04) \times 10^{-7}$ photon cm^{-2}s^{-1} for the component below 4 GeV corresponds to an apparent (isotropic) γ-ray luminosity of $L_\gamma(0.1 - 4\ \mathrm{GeV}) \simeq 10^{41}$ erg s^{-1}. The component above 4 GeV, on the other hand, is characterized by an isotropic HE luminosity of $L_\gamma(> 4\mathrm{GeV}) \simeq 1.4 \times 10^{40}$ erg s^{-1}. This is an order of magnitude less when compared with the first component, but still larger than the VHE luminosity reported by H.E.S.S. $L_\gamma(> 250\,\mathrm{GeV}) = 2.6 \times 10^{39}$ erg s^{-1} [5]. All luminosities are below the Eddington luminosity corresponding to the black hole mass in Cen A; nevertheless, they are still quite impressive when compared with the other nearby radio galaxy M87 containing a much more massive black hole.

Figure 5.3 shows the gamma-ray spectrum for the core of Cen A up to TeV energies. As one can see, the flux expected based on a power-law extrapolation of the low-energy component (below the break) clearly falls below the TeV flux reported by H.E.S.S.. Although the uncertainties in the photon

index are large, it is clear that the spectrum becomes harder above 4 GeV. Remarkably, a simple extrapolation of the second (above the break) high-energy component to TeV energies could potentially allow one to match the average H.E.S.S. spectrum. These spectral considerations support the conclusion that we may actually be dealing with two (or perhaps even more) components contributing to the HE gamma-ray core spectrum of Cen A. Our analysis of the HE light curves provides some weak indication for a possible variability on 45 day time scale, but the statistics are not sufficient to draw clear inferences.

The limited angular resolution ($\sim$ 5 kpc) and the lack of significant variability introduces substantial uncertainties as to the production site of the HE gamma-ray emission. In principle, the hard HE component could originate from both a very compact (sub-pc) and/or extended (multi-kpc) region(s). The double-peaked nuclear SED of Cen A has been reasonably well-modeled up to a few GeV in terms of SSC processes occurring in its inner jet [e.g., 18, 3]. In this context, the hardening on the HE spectrum above 4 GeV would indeed mark the appearance of a physically different component. This additional component could in principle be related to a number of different (not mutually exclusive) scenarios, such as (i) non-thermal processes in its black hole magnetosphere [45], (ii) multiple SSC-emitting components (i.e., differential beaming)[36] or (iii) photo-meson interactions of protons in the inner jet [33, 47], (iv) γ-ray induced pair-cascades in a torus-like region (at $\sim 10^3 r_s$) [e.g. 46] (v) secondary Compton up-scattering of host galaxy starlight [49] or (vi) inverse-Compton (IC) processes in the kpc-scale jet [e.g. 28]. What concerns the more compact scenarios (i)-(iv) just mentioned: Opacity considerations do not a priori exclude a near-BH-origin, but could potentially affect the spectrum towards highest energies [e.g. 44]. A SSC multi-blob VHE contribution, on the other hand, requires the soft gamma-rays to be due to synchrotron instead of IC processes, in which case correlated variability might be expected. Photo-meson ($p\gamma$) interactions with, e.g., UV or IR background photons (n_γ) require the presence of UHECR protons, which seems feasible for Cen A. However, as the mean free paths $\lambda \sim 1/(\sigma_{p\gamma} n_\gamma K_p)$ of protons through the relevant photon fields are comparatively large, usually only a modest fraction of the proton energy can be converted into secondary particles. Models of this type thus tend to need an injection power in high-energy protons exceeding the average jet power of $\sim 10^{43-44}$ erg/s [e.g. 58]. The efficiency of IC-supported pair cascades in Cen A, on the other hand, appears constrained by low accretion modes and the possible absence of a dust torus. Considering the more extended scenarios (v)-(vi): Partial absorption ($\sim$ 1%) of nuclear gamma-rays by starlight in the inner part of the host galaxy, and subsequent up-scattering of starlight photons could potentially introduce another HE contribution. However, the efficiency for this process is low, so that a high VHE injection power into the ambient medium is required, and the predicted spectral shape does not seem to match well. Compton-upscattering

of starlight photon by energetic electrons in the kpc-scale jet also seems to have difficulties in reproducing the noted HE characteristics.

Finally, let us mention that gamma-ray production may perhaps also be related to relativistic protons interacting with the ambient gas in the large (kpc) scale regions, e.g., the overall elliptical galaxy NGC 5128 or the densest part of its dust lane. Note that the γ-ray luminosity $\approx 10^{41}$ erg/s above 100 MeV is larger by two orders of magnitude than the γ-ray luminosity of the Milky Way, which could be related to a higher rate of cosmic-ray production and a more effective confinement in the case of NGC 5128. Moreover, gamma-rays might also be produced in a diluted $R_{\rm halo} \sim 30$ kpc (halo) region of this galaxy. Despite the low density of gas, gamma-ray production on characteristic timescale $t_{\rm pp} \approx 3 \times 10^9 (n/10^{-2}{\rm cm}^{-3})^{-1}$ yr can be effective, even for a relatively fast diffusion of cosmic rays in this region. More specifically, the efficiency could be close to one, if the diffusion coefficient at multi-GeV energies does not exceed $D \sim R_{\rm halo}^2/t_{\rm pp} \sim 10^{29}$ cm^2/s. This seems an interesting possibility, especially for the second (hard) HE component with photon index close to 2.1, in the context of its similarity to the gamma-ray spectrum of the so-called 'Fermi Bubbles' around the center of our Galaxy [51]. The much higher luminosity (by $\sim 2-3$ orders of magnitude) of the second component compared to the gamma-ray luminosity of the Fermi Bubbles seems quite natural, given the much larger energy available in Cen A, in particular in the form of kinetic energy of its jet.

The results presented here provide observational evidence for an additional contribution at the highest energies and a more complex spectral gamma-ray behavior than previously anticipated. While considerations like those mentioned above may lead one to favor one production scenario over the other, none of them cannot be easily discarded. In fact, it is well conceivable that several of them contribute to the observed gamma-ray emission. Definite progress in this regard could be achieved in case of a significant detection of gamma-ray time variability.

5.5 The lobes of Cen A

The data used for the study of γ-ray emission from the lobes of CenA are from the beginning of the operation until November 14, 2011, amounting to ~ 3 yr of data (MET 239557417– 342956687). We used the standard LAT analysis software (v9r23p1)[2]. To avoid systematic errors due to poor determination of the effective area at low energies, we selected only events with energies above 200 MeV. The region-of-interest (ROI) was selected to be a rectangular region of size $14^\circ \times 14^\circ$ centered on the position of Cen A (RA $= 201^\circ 21' 54''$, DEC $= -43^\circ 1' 9''$). To reduce the effect of Earth albedo backgrounds, time intervals

[2]http://fermi.gsfc.nasa.gov/ssc

when the Earth was appreciably in the FoV (specifically, when the center of the FoV was more than 52° from zenith) as well as time intervals when parts of the ROI were observed at zenith angles $> 105°$ were also excluded from the analysis. The spectral analysis was performed based on the P7v6 version of the post-launch instrument response functions (IRFs). We modeled the Galactic background component using the LAT standard diffuse background model *gal_2yearp7v6_v0* and we left the overall normalization and index as free parameters. We also used *iso_p7v6source* as the isotropic γ-ray background.
The resulting Fermi-LAT counts map for the 3 yr data set is shown in Figure 5.4(a). The (green) crosses show the position of the point-like sources from the 2FGL catalog ([40]) within the ROI. Extended emission to the north and south of Cen A is detected with significances of TS > 100 (10 σ) and TS > 400 (20 σ), respectively.

5.5.1 Spatial analysis

Events with energies between 200 MeV and 30 GeV were selected. The residual image after subtracting the diffuse background and point-like sources including the core of Cen A is shown in Figure 5.4(b). The fluxes and spectral indices of 11 other point-like sources generated from the 2FGL catalog within the ROI are also left as free parameters in the analysis. The 2FGL catalog source positions are shown in Figure 5.4(a), where 2FGL J1324.0-4330e accounts for the lobes (both north and south). A new point-like source (2FGL J1335.3-4058), located at RA $= 203°49'30'', \mathrm{DEC} = -40°34'48''$ accounts for some residual emission from the north lobe, although no known source at other wavelengths is found to be associated. We treat it as part of the north lobe here. The core of Cen A is modeled as a point-like source. Then the following steps were performed:

(1) To evaluate the total (extended) HE γ-ray emission we first used a template based on the residual map (T1; corresponding to the blue contours in Figure 5.5). The TS values for the south and the north lobe in this template are 411 and 155, respectively. The residual map was also compared with radio (WMAP, 22 GHz) lobe contours (green contours overlaid on Figure 5.4(b)). While lower-frequency radio maps exist, we expect the higher-frequency 22 GHz map to better represent the GeV-emitting particles. We find that the south lobe of the HE γ-ray image is similar to the south lobe of the radio one, whereas the HE emission in the north extends beyond the radio lobe emission region.
(2) To understand this feature better, we re-fitted the excess using an additional template (T2; red contours in Figure 5.6) generated from the radio (WMAP) image. The two templates are shown in Figure 5.5, and the corre-

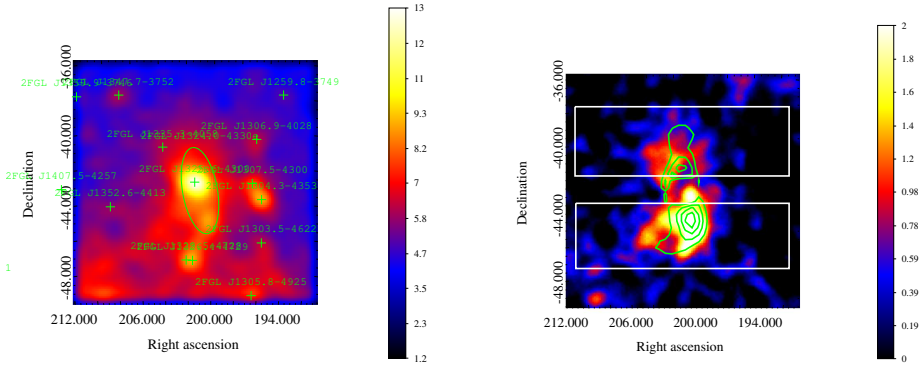

(a) LAT counts map of the 14° × 14° ROI. **(b)** Excess map after background subtraction.

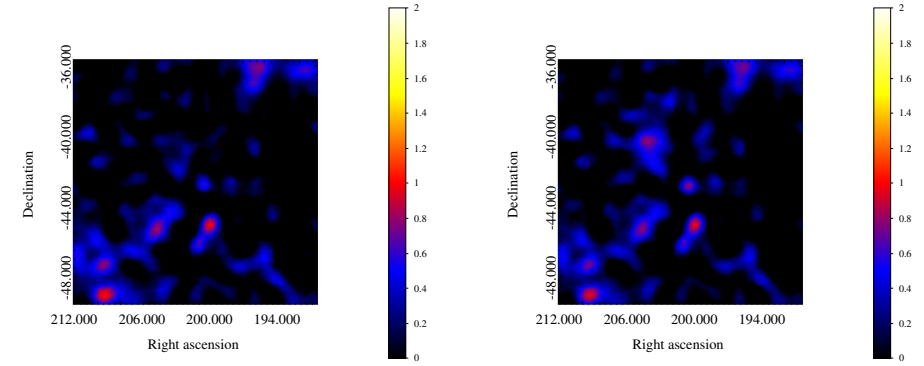

(c) Residual map for template T1. **(d)** Residual map for template T2.

Figure 5.4: The different maps for the Cen A region: (a) LAT counts map of the 14° × 14° region of interest (ROI) around the position of Cen A. The counts map is smoothed with a Gaussian of kernel 0.8°. The green crosses mark the position of the 2FGL point-like sources. (b) Excess map after subtraction of diffuse background, point-like sources and Cen A core. The contours are WMAP radio lobe contours, while the white boxes represent the projection regions discussed in Sec. 5.5.1. (c) Residual map using template T1 for the lobes. (d) Residual map using the radio template T2 for the lobes.

sponding residual maps are shown in Figure 5.4. While there is some residual emission to the north of Cen A for template T2, this residual emission is obviously absent from template T1. The qualitative features of the different residual maps are confirmed by the corresponding TS values, which are listed in Table 5.1. Accordingly, the HE south lobe seems to agree reasonably well with the radio south lobe, whereas for the north lobe, the template generated from the radio lobe (T2) fits the HE excess substantially worse than T1 (110 vs 155).

Table 5.1: TS value for the two templates used.

Model	north Lobe	south Lobe
T1	155	411
T2	110	406

(3) To further investigate a possible extension (or contribution of a background source) of the north lobe, we evaluated the projection of a rectangular region on the excess image (in white in Figure 5.4(b)). Figure 5.6 shows the projection for the north and south regions for Fermi-LAT image (in black) and the radio one (in red). The south projection for the radio map is well-fitted by a single Gaussian centered at ~ 0.05 (0 is defined as the center of the rectangle on $RA = 201°21'54'', DEC = -43°1'9''$) with an extension of $\sigma = 0.99°$. For the Fermi-LAT map the Gaussian is centered at ~ 0.5 and has $\sigma = 1.01°$, compatible with the radio map projection. In contrast, the north projection for the Fermi-LAT map has a Gaussian profile with $\sigma = 1.68°$, while for the radio map σ is 0.97°. The extension in the north projections for the Fermi-LAT map indicates that the γ-ray north lobe is more extended than the radio one or that an (otherwise unknown) source in the background may be contributing to the total emission.

5.5.2 Spectral analysis

Our morphological analysis indicates some incongruity between the morphology of the radio lobe and γ-ray lobe in the north. Hence, to model the γ-ray lobe as self-consistently as possible, we used the template generated with the residual map (T1). Integrating the whole γ-ray emission observed, we then derived the total flux and index in the 100 MeV to 30 GeV energy range. For the north lobe the integral HE flux is $(0.93 \pm 0.09) \times 10^{-7}$ph cm^{-2}s^{-1} and the photon index is 2.24 ± 0.08, while for the south lobe we find $(1.4 \pm 0.2) \times 10^{-7}$ph cm^{-2}s^{-1} and 2.57 ± 0.07, respectively. The results are summarized in Table 5.2, where the subscripts 3a and 10m refer to the three-year data (analyzed here) and the ten-month data (reported in [2]), respectively. We find

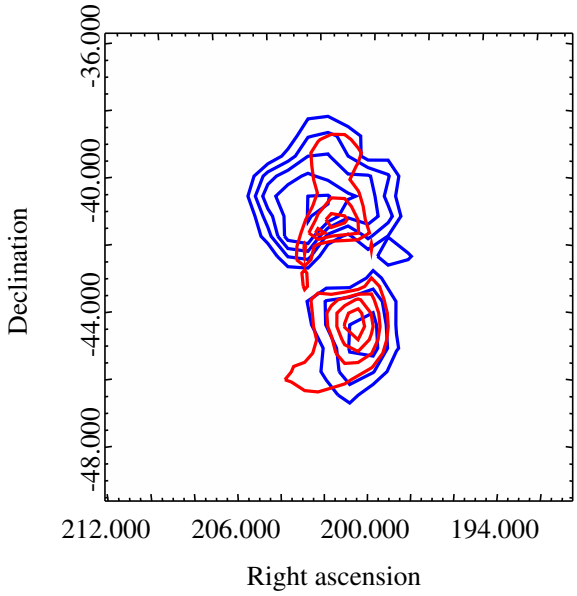

Figure 5.5: Two templates used in the analysis. The blue contours correspond to T1 and the red to T2.

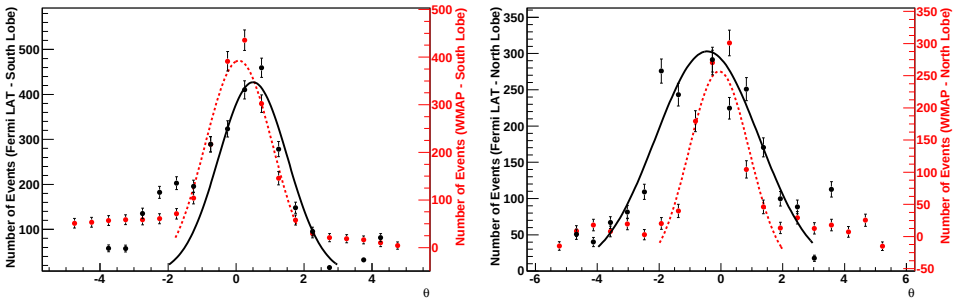

(a) Projection of the south lobe **(b)** Projection of the north lobe

Figure 5.6: Projection of the rectangular region shown in Figure 5.4(b) for both lobes. The curves are Gaussian fits, with WMAP data in red and Fermi-LAT data in black. Units for the positional (x) axis are degrees.

that the flux and photon indices in the T2 templates are similar to the ten-month data. On the other hand, the analysis using the T1 template results in a harder spectrum for the north lobe.
To derive the spectral energy distribution (SED) we divided the energy range into logarithmically spaced bands and applied *gtlike* in each of these bands. Only the energy bins for which a signal was detected with a significance of at least 2σ were considered, while an upper limit was calculated for those be-

low. As a result, there are seven bins in the SED for the south lobe.
To clarify the origin of the γ-ray emission, we evaluated the spectrum in different parts of each lobe. To this end, we divided each lobe into two parts and used *gtlike* to evaluate the spectrum. In the south lobe the resulting photon index is 2.8 ± 0.2 near the Cen A core and 2.3 ± 0.1 far away from the core. Unfortunately, the statistics are still not high enough to claim a clear hardening of the spectrum. For the northern lobe, both parts appear to be consistent with values of 2.2 ± 0.2.

Table 5.2: Fluxes and spectra of the lobes

Source Name	Φ_{3a}(T1)	Γ_{3a}(T1)	Φ_{10m}	Γ_{10m}	Φ_{3a}(T2)	Γ_{3a}(T2)
South Lobe	1.43 ± 0.15	2.57 ± 0.07	1.09 ± 0.24	2.60 ± 0.15	1.40 ± 0.15	2.56 ± 0.08
North Lobe	0.93 ± 0.09	2.24 ± 0.08	0.77 ± 0.20	2.52 ± 0.16	0.64 ± 0.15	2.56 ± 0.08

Φ is the integral flux (100 MeV to 30 GeV) in units of $10^{-7}\mathrm{ph} \cdot \mathrm{cm}^{-2}\mathrm{s}^{-1}$ and Γ is the photon index. The subscripts "3a" and "10m" refer to the three-year data analyzed here and to the ten-month results (based on a WMAP template) reported in [2], respectively.

5.6 The origin of the non-thermal lobe emission

Using the WMAP and Fermi-LAT results reported here, we can characterize the spectral energy distributions for the north and the south lobe. While the radio emission is usually taken to be caused by electron synchrotron emission, the origin of the HE γ-ray emission could in principle be related to both leptonic (inverse-Compton scattering) and hadronic (e.g., pp-interaction) processes. In the following we discuss possible constraints for the underlying radiation mechanism as imposed by the observed SEDs.

5.6.1 Inverse-Compton origin of γ-rays

Both the HE γ-ray and the radio emission could be accounted for in a leptonic scenario. In the simplest version, a single population of electrons $N(\gamma, t)$ is used to model the SED through synchrotron and inverse-Compton emission, with particle acceleration being implicitly treated by an effective injection term $Q = Q(\gamma, t)$. The latter allows us to distinguish acceleration caused by, e.g., multiple shocks or stochastic processes (e.g., [41]) from emission, and enables a straightforward interpretation. The kinetic equation describing the energetic and temporal evolution of the radiating electrons can then be written as

$$\frac{\partial N}{\partial t} = \frac{\partial}{\partial \gamma}\left(P\,N\right) - \frac{N}{\tau_{esc}} + Q\,, \tag{5.6.1}$$

where $P = P(\gamma) = -\frac{d\gamma}{dt}$ is the (time-independent) energy loss rate and $\tau_{\rm esc}$ is the characteristic escape time. For negligible escape (as appropriate here, given the large size of the γ-ray emitting region) and quasi continuous injection (considered as a suitable first-order approximation given the short lifetime of TeV electrons and the scales of the lobes) $Q(\gamma, t) = Q(\gamma)$, the solution of the kinetic equation becomes

$$N(\gamma, t) = \frac{1}{P(\gamma)} \int_{\gamma}^{\gamma_0} Q(\gamma) d\gamma \, , \tag{5.6.2}$$

where γ_0 is found by solving the characteristic equation for a given epoch t, $t = \int_{\gamma}^{\gamma_0} \frac{d\gamma}{P(\gamma)}$ (e.g., [11]). If synchrotron or inverse-Compton (Thomson) losses ($P(\gamma) = a\,\gamma^2$) provide the dominant loss channel, then $\gamma_0 = \gamma/(1 - a\gamma t)$, so that at the energy $\gamma_{\rm br} = \frac{1}{a\,t}$ the stationary power-law electron injection spectrum steepens by a factor of 1 (cooling break) due to radiative losses, naturally generating a broken power-law.
We used the above particle distribution described in eq. (5.6.2) for a representation of the observed lobe SEDs. The magnetic field strength B, the maximum electron energy $\gamma_{\rm max}$ and the epoch time t were left as free parameters to model the data. Klein-Nishina (KN) effects on the inverse-Compton-scattered HE spectrum were taken into account (following [6]).
Figure 5.7 shows the SED results obtained for the north and south lobes. The HE part of both spectra can be described by a power-law with photon index $\Gamma_\gamma \simeq 2.2$ and 2.6 for the north and the south lobe, respectively. At low energies, the south lobe spectrum shows a synchrotron peak at about 5 GHz, while the north lobe is well described by a power-law with an index > 2. Note that if one would use a simple power-law electron injection spectrum $Q(\gamma) \propto \gamma^{-\alpha}$, evolving in time with a cooling break, to describe the HE γ-ray spectrum, a power index $\alpha = 3.2$ would be required for the south lobe. Yet, assuming that the same electron population is responsible for both the radio-synchrotron and HE inverse-Compton emission, such a value would be in conflict with the results obtained from the WMAP data analysis, indicating an electron population with power-law index $\alpha \simeq 2$ based on the detected synchrotron emission. As it turns out, however, this problem could be accommodated by considering a more natural spectral input shape, e.g., an electron injection spectrum with an exponential cut-off

$$Q(\gamma) = Q_0\, \gamma^{-\alpha} \exp\left(-\frac{\gamma}{\gamma_{\rm max}}\right) , \tag{5.6.3}$$

where the constant Q_0 can be obtained from the normalization to the injection power $L = m_e c^2 \int Q(\gamma)\, \gamma\, d\gamma$.
The age of the giant lobe emission, and associated with this, the duration of particle acceleration activity, is somewhat uncertain. Dynamical arguments

suggest a lower limit $> 10^7$ yr for the giant radio lobes, while synchrotron spectral aging arguments indicate an age $\lesssim 3 \times 10^7$ yr (e.g., [32, 9, 27]). The observed GeV extension in itself would already imply an extreme lower limit of $R/c > 10^6$ yr. In the following we therefore discuss the SED implications for an epoch time t between 10^7 yr and 10^8 yr. As it turns out, the modeling of the GeV data provides support for a maximum lobe age of $\sim 8 \times 10^7$ yr.
For the south lobe, the radio data suggest a break frequency $\nu_{\rm br} = 5$ GHz above which the spectrum drops abruptly. The break in the synchrotron spectrum is related to the break in the electron spectrum via $\nu_{\rm br} = 1.3\,\gamma_{\rm br}^2\,B_{1\mu G}$ Hz. In principle, a change in the spectral shape of the electron population might be caused by cooling effects or/and the existence of a maximum energy for the electron population. For a minimum epoch time $t_{\rm min} = 10^7$ yr, cooling would affect the synchrotron spectrum at frequency $\approx 80 B_{1\mu G}$ GHz, much higher than inferred from the radio data. Therefore, to obtain a break at 5 GHz in the south lobe, a maximum energy in the electron population ($\gamma_{\rm max}$), lower than $\gamma_{\rm br}$ defined by $t = t_{\rm min}$ would be needed. On the other hand, for a maximum epoch time $t_{\rm max} = 8 \times 10^7$ yr, the power-law spectral index changes at frequency $\simeq 1 B_{1\mu G}$ GHz, providing a satisfactory agreement with the radio data. In this case the maximum electron energy is obtained from the radio data above the break frequency 5 GHz. Results for the considered minimum and maximum epoch time, and for a fixed power-law electron index $\alpha = 2$ are illustrated in Figures 5.7 and 5.8. Note that for $B \leq 3\mu$G, the energy loss rate $P(\gamma)$ is dominated by the IC channel only, so that the results of the calculations are quite robust.
Figure 5.7 shows a representation of the SED for the north and the south lobe, respectively, using the parameters $t_{\rm min} = 10^7$ yr and $\gamma_{\rm max} = 1.5 \times 10^5$. The dashed line shows the HE contribution produced by inverse-Compton scattering of cosmic microwave background photons by relativistic electrons within the lobes. In this case the resulting γ-ray flux can only describe the first two data points and then drops rapidly. Consequently, to be able to account for the observed HE spectrum, extragalactic background light photons need to be included in addition to CMB photons (see dot-dashed line in Figure 5.7). Upscattering of infrared-to-optical EBL photons was already required in the stationary leptonic model reported in the original Fermi paper ([2]). In our approach we adopt the model by [24] to evaluate this EBL contribution. The solid line in Figure 5.7 represents the total (CMB+EBL) inverse-Compton contribution. The maximum total energy of electrons in both lobes is found to be $\sim 2 \times 10^{58}$ erg and the energy in the magnetic fields is roughly 25% of this. Dividing the total energy by the epoch time 10^7 yr would imply a mean kinetic power of the jets inflating the lobes of $\simeq 7 \times 10^{43}$ erg/s, roughly two orders of magnitude lower than the Eddington power inferred for the black hole mass in Cen A, yet somewhat above the estimated power of the kpc-scale jet in the current epoch of jet activity ([20]). This could indicate that the jet was more powerful in the past. Obviously, the requirement on the mean jet

power can be significantly reduced if one assumes an older age of the lobes. Figure 5.8 shows a representation of the SED for an epoch time $t_{\rm max} = 8 \times 10^7$ yr, with a maximum electron Lorentz factor $\gamma_{\rm max} = 2.5 \times 10^6$ and 1.5×10^6 for the north lobe and the south lobe, respectively. Note that in this case the contribution by inverse-Compton scattering of CMB photons alone is sufficient to account for the observed HE spectrum (see the solid line in Figure 5.8). The inverse-Compton contribution of EBL photons only becomes important at higher energies (see the dot-dashed line in Figure 5.8). On the other hand, for an epoch time t exceeding $t_{\rm max} = 8 \times 10^7$ yr, the high-energy part of the SED would no longer be consistent with the data (see the dashed line in Figure 5.8 for $t = 10^8$ yr). This could be interpreted as additional evidence for a finite age $< 10^8$ yr of the lobes. The maximum total energy of electrons in both lobes is found to be $\approx 6 \times 10^{57}$ erg, with the total energy in particles and fields comparable to the 10^7yr-case, thus requiring only a relatively modest mean kinetic jet power of $\sim 10^{43}$ erg/s.

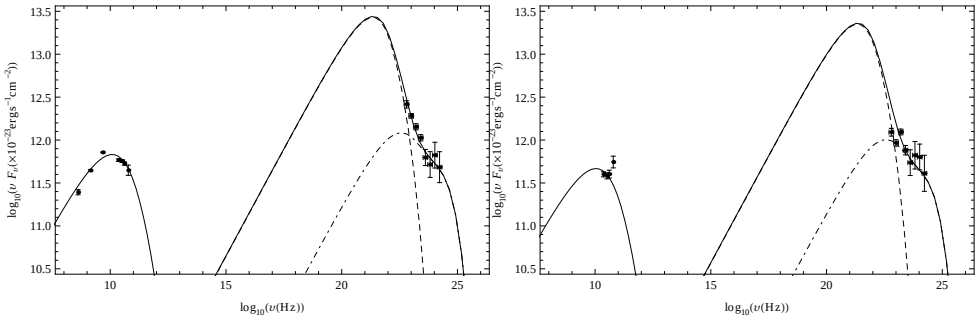

(a) South lobe **(b)** γ-ray excess (lobe) region in the north

Figure 5.7: Synchrotron and inverse-Compton fluxes for $t = 10^7$ yr. The radio data for the south lobe are from [27] (sum of region 4 and region 5 in their Table 1), while the radio data for the north region are from the WMAP analysis in this paper. The mean magnetic field value B used for the north and the south lobe is 0.39 μG and 0.43 μG, respectively. The dot-dashed line refers to the IC contribution due to EBL upscattering.

5.6.2 Hadronic γ-rays?

Once protons are efficiently injected, they are likely to remain energetic since the cooling time for pp-interactions is $t_{\rm pp} \approx 10^{15}(n/1\ cm^{-3})^{-1}$ s. High-energy protons interacting with the ambient low-density plasma can then produce daughter mesons and the π^0 component decays into two γ-rays. The data reported here allow us to derive an upper limit on the energetic protons contained in the lobes of Cen A. As before, we use a power-law proton distri-

bution with an exponential cut-off, i.e.,

$$N(\gamma_p) = N_0\ \gamma_p^{-\alpha} \exp\left(-\frac{\gamma_p}{\gamma_{\rm max}}\right)$$

where the constant N_0 can be expressed in terms of the total proton energy $W_p = m_p c^2 \int \gamma_p\ N(\gamma_p)\, d\gamma_p$. Current estimates for the thermal plasma density in the giant radio lobes of Cen A suggest a value in the range $n \simeq (10^{-5} - 10^{-4})$ cm^{-3} (e.g., [31, 22]). We used $n = 10^{-4}$ cm^{-3} for the model representation shown in dotted line in Figure 5.8. In both lobes, the power-law index of the proton population is $\alpha = 2.1$, and the high-energy cut-off is $E_{\rm max} \simeq 55$ GeV. The maximum total energy W_p is proportional to the gas number density n, so that $W_p \simeq 10^{61}(n/10^{-4}\ {\rm cm}^{-3})^{-1}$ erg, obtained here, should be considered as an upper limit. In principle, protons could be accumulated over the whole evolutionary timescale of the lobes. For a long timescale of $\geq 10^9$ yr, an average injection power $\leq 3 \times 10^{44}$ erg/s and a mean cosmic-ray diffusion coefficient of $D \sim R^2/t \lesssim 3 \times 10^{30}(R/100\ {\rm kpc})^2$ cm^2/s would be needed.

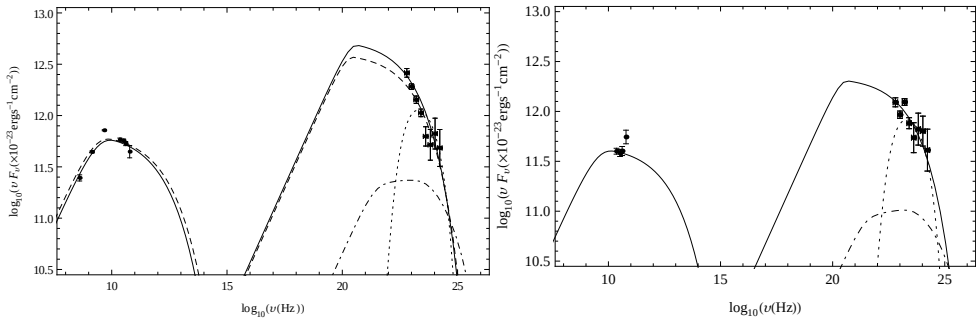

(a) South lobe **(b)** γ-ray excess (lobe) region in the north

Figure 5.8: Synchrotron and inverse-Compton fluxes for $t = 8 \times 10^7$ yr. The mean magnetic field value B for the south lobe and the γ-ray excess region in the north lobe is 0.91 μG and 1.17 μG, respectively. The dot-dashed line refers to the IC contribution due to EBL upscattering. The dashed line (a) shows the result for $t = 10^8$ yr. The possible γ-ray flux expected from pp-interactions for a thermal gas density $n = 10^{-4}\ cm^{-3}$ are also shown (dotted line).

5.7 Discussion and conclusion-2

Results based on an detailed analysis of 3 yr of Fermi-LAT data on the giant radio lobes of Cen A shows that they are detected with a significance more than twice as high as reported before (i.e., with more than 10 and 20σ for the northern and the southern lobe, respectively) which allows a better

determination of their spectral features and morphology. A comparison of the Fermi-LAT data with WMAP data indicates that the HE γ-ray emission regions do not fully coincide with the radio lobes. There is of course no a priori reason for them to coincide. The results reported here particularly support a substantial HE γ-ray extension beyond the WMAP radio image for the northern lobe of Cen A. We have reconstructed the SED based on data from the same emission region. A satisfactory representation is possible in a time-dependent leptonic scenario with radiative cooling taken into account self-consistently and injection described by a single power-law with exponential cut-off. The results imply a finite age $< 10^8$ yr of the lobes and a mean magnetic field strength $B \lesssim 1\mu$G. While for lobe lifetimes on the order of 8×10^7 yr, inverse-Compton up-scattering of CMB photons alone would be sufficient to account for the observed HE spectrum, up-scattering of EBL photons is needed for shorter lobe lifetimes. In a leptonic framework, the HE emission directly traces (via inverse-Compton scattering) the underlying relativistic electron distribution and thereby provides a spatial diagnostic tool. The radio emission, arising from synchrotron radiation, on the other hand also traces the magnetic field distribution. Together, the HE γ-ray and the radio emission thus offer important insights into the physical conditions of the source. That the HE emission seems extended beyond the radio image could then be interpreted as caused by a change in the magnetic field characterizing the region. This would imply that our quasi-homogeneous SED model for the HE lobes can only serve as a first-order approximation and that more detailed scenarios need to be constructed to fully describe the data. This also applies to the need of incorporating electron re-acceleration self-consistently. Extended HE emission could in principle also be related to a contribution from hadronic processes. The cooling timescales for protons appear much more favorable. On the other hand, both the spectral shape of the lobes and the required energetics seem to disfavor pp-interaction processes as sole contributor.

Bibliography

[1] R. Abbasi, Y. Abdou, T. Abu-Zayyad, et al.
Time-integrated Searches for Point-like Sources of Neutrinos with the 40-string IceCube Detector.
ApJ, 732:18, May 2011.

[2] A. A. Abdo, M. Ackermann, M. Ajello, et al.
Fermi Gamma-Ray Imaging of a Radio Galaxy.
Science, 328:725–, May 2010.

[3] A. A. Abdo, M. Ackermann, M. Ajello, et al.
Fermi Large Area Telescope View of the Core of the Radio Galaxy Centaurus A.
ApJ, 719:1433–1444, August 2010.

[4] F. Aharonian, L. Anchordoqui, D. Khangulyan, and T. Montaruli.
Microquasar LS 5039: a TeV gamma-ray emitter and a potential TeV neutrino source.
Journal of Physics Conference Series, 39:408–415, May 2006.

[5] **F. Aharonian**, A. G. Akhperjanian, G. Anton, et al.
Discovery of Very High Energy γ-Ray Emission from Centaurus a with H.E.S.S.
ApJL, 695:L40–L44, April 2009.

[6] **F. Aharonian** and A. M. Atoyan.
Compton scattering of relativistic electrons in compact X-ray sources.
Ap&SS, 79:321–336, October 1981.

[7] J. Ahrens, J. N. Bahcall, X. Bai, et al.
Sensitivity of the IceCube detector to astrophysical sources of high energy muon neutrinos.
Astroparticle Physics, 20:507–532, February 2004.

[8] J. Aleksić, L. A. Antonelli, P. Antoranz, et al.
Magic Constraints on γ-ray Emission from Cygnus X-3.
ApJ, 721:843–855, September 2010.

[9] H. Alvarez, J. Aparici, J. May, and P. Reich.
The radio continuum spectrum of Centaurus A's large-scale components.

A&A, 355:863–872, March 2000.

[10] A. T. Araudo, V. Bosch-Ramon, and G. E. Romero.
High-energy emission from jet-clump interactions in microquasars.
A&A, 503:673–681, September 2009.

[11] A. M. Atoyan and **F. Aharonian**.
Modelling of the non-thermal flares in the Galactic microquasar GRS 1915+105.
MNRAS, 302:253–276, January 1999.

[12] W. B. Atwood, A. A. Abdo, M. Ackermann, et al.
The Large Area Telescope on the Fermi Gamma-Ray Space Telescope Mission.
ApJ, 697:1071–1102, June 2009.

[13] P. Baerwald and D. Guetta.
Estimation of the Neutrino Flux and Resulting Constraints on Hadronic Emission Models for Cyg X-3 Using AGILE Data.
ApJ, 773:159, August 2013.

[14] E. E. Becklin, G. Neugebauer, F. J. Hawkins, K. O. Mason, P. W. Sanford, K. Matthews, and C. G. Wynn-Williams.
Infrared and X-ray Variability of Cyg X-3.
Nature, 245:302–304, October 1973.

[15] J. M. Bonnet-Bidaud and G. Chardin.
Cygnus X-3, a critical review.
Phys. Rep., 170:325–404, December 1988.

[16] A. Bulgarelli, M. Tavani, A. W. Chen, et al.
AGILE detection of Cygnus X-3 γ-ray active states during the period mid-2009/mid-2010.
A&A, 538:A63, February 2012.

[17] B. Cerutti, G. Dubus, J. Malzac, A. Szostek, R. Belmont, A. A. Zdziarski, and G. Henri.
Absorption of high-energy gamma rays in Cygnus X-3.
A&A, 529:A120, May 2011.

[18] M. Chiaberge, A. Capetti, and A. Celotti.
The BL Lac heart of Centaurus A.
MNRAS, 324:L33–L37, July 2001.

[19] S. Corbel, G. Dubus, J. A. Tomsick, et al.
A giant radio flare from Cygnus X-3 with associated γ-ray emission.
MNRAS, 421:2947–2955, April 2012.

[20] J. H. Croston, R. P. Kraft, M. J. Hardcastle, et al.
High-energy particle acceleration at the radio-lobe shock of Centaurus A.
MNRAS, 395:1999–2012, June 2009.

[21] G. Dubus, B. Cerutti, and G. Henri.
The relativistic jet of Cygnus X-3 in gamma-rays.
MNRAS, 404:L55–L59, May 2010.

[22] I. J. Feain, R. D. Ekers, T. Murphy, et al.
Faraday Rotation Structure on Kiloparsec Scales in the Radio Lobes of Centaurus A.
ApJ, 707:114–125, December 2009.

[23] Fermi LAT Collaboration, A. A. Abdo, M. Ackermann, et al.
Modulated High-Energy Gamma-Ray Emission from the Microquasar Cygnus X-3.
Science, 326:1512–, December 2009.

[24] A. Franceschini, G. Rodighiero, and M. Vaccari.
Extragalactic optical-infrared background radiation, its time evolution and the cosmic photon-photon opacity.
A&A, 487:837–852, September 2008.

[25] R. Giacconi, P. Gorenstein, H. Gursky, and J. R. Waters.
An X-Ray Survey of the Cygnus Region.
ApJL, 148:L119, June 1967.

[26] R. J. Gould and G. P. Schréder.
Pair Production in Photon-Photon Collisions.
Physical Review, 155:1404–1407, March 1967.

[27] M. J. Hardcastle, C. C. Cheung, I. J. Feain, and Ł. Stawarz.
High-energy particle acceleration and production of ultra-high-energy cosmic rays in the giant lobes of Centaurus A.
MNRAS, 393:1041–1053, March 2009.

[28] M. J. Hardcastle and J. H. Croston.
Modelling TeV γ-ray emission from the kiloparsec-scale jets of Centaurus A and M87.
MNRAS, 415:133–142, July 2011.

[29] R. C. Hartman, D. L. Bertsch, and S. D. Bloom.
The Third EGRET Catalog of High-Energy Gamma-Ray Sources.
ApJSS, 123:79–202, July 1999.

[30] IceCube Collaboration, R. Abbasi, Y. Abdou, M. Ackermann, J. Adams, J. A. Aguilar, M. Ahlers, D. Altmann, K. Andeen, J. Auffenberg, and et al.
Searches for High-energy Neutrino Emission in the Galaxy with the Combined ICECUBE-AMANDA Detector.
ApJ, 763:33, January 2013.

[31] N. Isobe, K. Makishima, M. Tashiro, and H. Kaneda.
ASCA observations of the northern outer lobe edge of the radio galaxy Centaurus A.
In R. A. Laing and K. M. Blundell, editors, *Particles and Fields in Radio Galaxies Conference*, volume 250 of *Astronomical Society of the Pacific Conference Series*, page 394, 2001.

[32] F. P. Israel.
Centaurus A - NGC 5128.
A&AR, 8:237–278, 1998.

[33] M. Kachelrieß, S. Ostapchenko, and R. Tomàs.
TeV Gamma Rays from Ultrahigh Energy Cosmic Ray Interactions in the Cores of Active Galactic Nuclei: Lessons from Centaurus A.
PASA, 27:482–489, October 2010.

[34] S. R. Kelner, F. A. Aharonian, and V. V. Bugayov.
Energy spectra of gamma rays, electrons, and neutrinos produced at proton-proton interactions in the very high energy regime.
Phys. Rev. D, 74(3):034018, August 2006.

[35] K. I. I. Koljonen, D. C. Hannikainen, M. L. McCollough, G. G. Pooley, and S. A. Trushkin.
The hardness-intensity diagram of Cygnus X-3: revisiting the radio/X-ray states.
MNRAS, 406:307–319, July 2010.

[36] J.-P. Lenain, C. Boisson, H. Sol, and K. Katarzyński.
A synchrotron self-Compton scenario for the very high energy γ-ray emission of the radiogalaxy M 87. Unifying the TeV emission of blazars and other AGNs?
A&A, 478:111–120, January 2008.

[37] Z. Ling, S. N. Zhang, and S. Tang.
Determining the Distance of Cyg X-3 with its X-Ray Dust Scattering Halo.
ApJ, 695:1111–1120, April 2009.

[38] C. Ma, E. F. Arias, T. M. Eubanks, et al.

The International Celestial Reference Frame as Realized by Very Long Baseline Interferometry.
AJ, 116:516–546, July 1998.

[39] A. J. Mioduszewski, M. P. Rupen, R. M. Hjellming, G. G. Pooley, and E. B. Waltman.
A One-sided Highly Relativistic Jet from Cygnus X-3.
ApJ, 553:766–775, June 2001.

[40] P. L. Nolan, A. A. Abdo, M. Ackermann, M. Ajello, A. Allafort, E. Antolini, W. B. Atwood, M. Axelsson, L. Baldini, J. Ballet, and et al.
Fermi Large Area Telescope Second Source Catalog.
ApJSS, 199:31, April 2012.

[41] S. O'Sullivan, B. Reville, and A. M. Taylor.
Stochastic particle acceleration in the lobes of giant radio galaxies.
MNRAS, 400:248–257, November 2009.

[42] D. R. Parsignault, H. Gursky, E. M. Kellogg, et al.
Observations of Cygnus X-3 by Uhuru.
Nature Physical Science, 239:123–125, October 1972.

[43] G. Piano, M. Tavani, V. Vittorini, et al.
The AGILE monitoring of Cygnus X-3: transient gamma-ray emission and spectral constraints.
A&A, 545:A110, September 2012.

[44] F. M. Rieger.
Nonthermal Processes in Black Hole-Jet Magnetospheres.
International Journal of Modern Physics D, 20:1547–1596, 2011.

[45] F. M. Rieger and **F. Aharonian**.
Centaurus A as TeV γ-ray and possible UHE cosmic-ray source.
A&A, 506:L41–L44, November 2009.

[46] P. Roustazadeh and M. Böttcher.
Very High Energy Gamma-ray-induced Pair Cascades in the Radiation Fields of Dust Tori of Active Galactic Nuclei: Application to Cen A.
ApJ, 728:134, February 2011.

[47] S. Sahu, B. Zhang, and N. Fraija.
Hadronic-origin TeV γ rays and ultrahigh energy cosmic rays from Centaurus A.
Phys. Rev. D, 85(4):043012, February 2012.

[48] P. Sreekumar, D. L. Bertsch, R. C. Hartman, P. L. Nolan, and D. J. Thompson.

GeV emission from the nearby radio galaxy Centaurus A.
Astroparticle Physics, 11:221–223, June 1999.

[49] Ł. Stawarz, **F. Aharonian**, S. Wagner, and M. Ostrowski.
Absorption of nuclear γ-rays on the starlight radiation in FR I sources: the case of Centaurus A.
MNRAS, 371:1705–1716, October 2006.

[50] H. Steinle, K. Bennett, H. Bloemen, W. Collmar, R. Diehl, W. Hermsen, G. G. Lichti, D. Morris, V. Schonfelder, A. W. Strong, and O. R. Williams.
COMPTEL observations of Centaurus A at MeV energies in the years 1991 to 1995.
A&A, 330:97–107, February 1998.

[51] M. Su, T. R. Slatyer, and D. P. Finkbeiner.
Giant Gamma-ray Bubbles from Fermi-LAT: Active Galactic Nucleus Activity or Bipolar Galactic Wind?
ApJ, 724:1044–1082, December 2010.

[52] A. Szostek and A. A. Zdziarski.
Effects of the stellar wind on X-ray spectra of Cygnus X-3.
MNRAS, 386:593–607, May 2008.

[53] A. Szostek, A. A. Zdziarski, and M. L. McCollough.
A classification of the X-ray and radio states of Cyg X-3 and their long-term correlations.
MNRAS, 388:1001–1010, August 2008.

[54] M. Tavani, A. Bulgarelli, G. Piano, et al.
Extreme particle acceleration in the microquasar CygnusX-3.
Nature, 462:620–623, December 2009.

[55] V. Tudose, J. C. A. Miller-Jones, R. P. Fender, et al.
Probing the behaviour of the X-ray binary Cygnus X-3 with very long baseline radio interferometry.
MNRAS, 401:890–900, January 2010.

[56] M. H. van Kerkwijk, P. A. Charles, T. R. Geballe, et al.
Infrared helium emission lines from Cygnus X-3 suggesting a Wolf-Rayet star companion.
Nature, 355:703–705, February 1992.

[57] O. Vilhu, P. Hakala, D. C. Hannikainen, M. McCollough, and K. Koljonen.
Orbital modulation of X-ray emission lines in Cygnus X-3.
A&A, 501:679–686, July 2009.

[58] R.-Z. Yang, **N. Sahakyan**, E. de Ona Wilhelmi, **F. Aharonian**, and F. Rieger.
Deep observation of the giant radio lobes of Centaurus A with the Fermi Large Area Telescope.
A&A, 542:A19, June 2012.

[59] A. A. Zdziarski, M. Sikora, G. Dubus, F. Yuan, B. Cerutti, and A. Ogorzałek.
The gamma-ray emitting region of the jet in Cyg X-3.
MNRAS, 421:2956–2968, April 2012.